Insight into discharge of non-aqueous Li–O$_2$ battery using a three-dimensional electrochemical lattice Boltzmann model

Timan Lei [a], Junyu Yang [a], Geng Wang [b], Jin Chen [a], Yinglong He [c], Kai H. Luo [a,d,*]

[a] *Department of Mechanical Engineering, University College London, Torrington Place, London WC1E 7JE, UK*
[b] *National Microgravity Laboratory, Institute of Mechanics, Chinese Academy of Sciences, Beijing 100190, China*
[c] *School of Mechanical Engineering Sciences, University of Surrey, Guildford, GU2 7XH, UK*
[d] *Shanghai Institute for Advanced Study, Zhejiang University, Shanghai 201203, China*

ARTICLE INFO

ABSTRACT

Non-aqueous Li–O$_2$ battery (NALiO2B) is a promising alternative to lithium-ion batteries, offering high theoretical energy density. However, its practical applications are hampered by limited understanding of the underlying mechanisms. In this study, a three-dimensional electrochemical lattice Boltzmann method is proposed to simulate the physical and electrochemical processes during NALiO2B discharge at the pore scale. The discharge performance of NALiO2B is evaluated for various electrode and electrolyte designs. It is found that the limited O$_2$ diffusion within homogeneous electrodes is the primary cause of the declined reactive electrode surface area, the intensified electrochemical reaction (or overpotential), and finally the premature battery death. This issue can be mitigated by employing the hierarchical electrode BP$_2$ with a bi-porous structure. The large pores in BP$_2$ improve O$_2$ transport to sustain the continuous electrochemical reaction process, thus enhancing the discharge capacity of NALiO2B. To further boost the rate capability of NALiO2B, BP$_2$ is partially infiltrated with electrolyte to form the multiphase (MP) electrode, where air bubbles exist and serve as O$_2$ reservoirs. These bubbles effectively provide adequate O$_2$ to support the extensive O$_2$ consumption during the fast electrochemical reaction at high current densities. Consequently, NALiO2B with MP demonstrates the satisfactory discharge capacity and rate capability. This study provides valuable insights into the complex physics and reaction kinetics behind NALiO2B discharge, which facilitates the optimization and development of NALiO2B.

1. Introduction

The rapid development of electric vehicles (EVs) boosts the demand for high-performance batteries beyond the lithium-ion battery (LiB) [1–3]. A promising candidate is the rechargeable Li–O$_2$ battery (LiO2B) that consists of three key components: metal Li anode, separator, and porous air cathode [4–6]. The cathode active material O$_2$ is freely sourced from ambient air, thereby minimizing the weight and volume of cathode. Meanwhile, the Li anode ensures the high discharge capacity and cell voltage. These two factors contribute to the extremely high theoretical energy density of LiO2B (∼3500 Wh/kg), in contrast to around 300 Wh/kg of LiB. This makes LiO2B a promising alternative technology to satisfy future EVs' soaring demand for high-power energy storage systems [7–9].

One of the first attempts to construct an LiO2B was made by Abraham and Jiang in 1996, where a solid polymer electrolyte was applied to show the battery rechargeability with good coulombic efficiency [10,11]. Extensive research was then conducted to explore different LiO2Bs

architectures with aqueous (water-based liquid), non-aqueous (aprotic liquid), solid-state, or hybrid (solid and liquid) electrolytes [12]. Among these battery systems, the non-aqueous LiO2B (NALiO2B) attracted global research interest, driven by its promising energy density and capacity, exceptional cycle life, and simple construction [13–15]. Generally, the electrochemical reaction of NALiO2B is described as, $2\text{Li} + \text{O}_2 \leftrightarrow \text{Li}_2\text{O}_2 \ (E^0 = 2.96 \text{ V})$. The insoluble and insulating Li$_2$O$_2$ on cathode surfaces, combined with the slow O$_2$ transport within the electrolyte, can result in sluggish reaction kinetics and concomitant poor performance, such as high overpotential, low capacity and rate capability, and reduced cycle life [16–18]. Therefore, to which extent NALiO2B can deliver on its potential relies on the electrochemical reaction behaviors.

Experiments were carried out to develop new cathode structures aimed at improving the reaction process and thus enhancing the performance of NALiO2B [19,20]. Kushima et al. observed floating Li$_2$O$_2$

---

particles in electrolyte at low discharge potential (or high overpotential), which led to the irreversible capacity loss and cyclability decline of NALiO2B. They suggested using electrodes with pores in different sizes to help address this issue [21]. Hierarchical electrode structures were emphasized for their ability to reduce the surface deposition of Li_2O_2, thereby improving the discharge capacity of NALiO2B [22]. Kim et al. also verified the cathode porosity could influence O_2 and Li^+ transport, Li_2O_2 formation and decomposition, and finally the NALiO2B performance, i.e., the meso-porous cathode showed a higher battery capacity but a limited cycle life compared to the micro-porous cathode [23]. A meso-porous electrode, featuring small volume and large surface area, was synthesized by Dutta et al. to direct the formation of one-dimensional (1D) and amorphous Li_2O_2, resulting in a significant improvement in round-trip efficiency of NALiO2B to 80% [24]. They demonstrated that the slow O_2 transport was the key factor destabilizing the reaction process and causing the rapid discharge capacity decline at high current densities. This issue could be mitigated by adjusting the electrode surface area, porosity, and thickness, as well as the O_2 concentration and diffusion coefficient [25]. Additionally, experimental efforts were made to investigate working conditions for optimizing the performance of NALiO2B. Changes in electrolyte solutions were shown to modify the growth pathways (i.e., surface electrochemistry or solution disproportionation reaction) and morphologies (i.e., dense film or porous structure) of Li_2O_2, thus controlling the discharge capacity of NALiO2B [14]. The solution and surface pathways were then reported to dominate the discharge of NALiO2B at $-20 \sim 0\ °C$ and $0 \sim 40\ °C$, respectively [26]. Mediators were introduced to promote Li_2O_2 formation in solution and thereby increase NALiO2B capacity by 80–100 times [27,28]. Electrolyte materials were adjusted to prevent side reactions and reach a long cycle life of NALiO2B in an air-like atmosphere [29]. An NALiO2B incorporating CO_2 was developed to reach a full discharge capacity of 6628 mAh/g for 715 cycles [30].

Existing experimental findings have emphasized the critical role of optimal battery architectures and working conditions in optimizing the electrochemical reaction process and enhancing the performance of NALiO2B. However, due to the expensive and time-consuming nature of experiments, only a limited number of battery designs were explored experimentally. Consequently, the numerical modeling has emerged as an efficient tool for studying the complex physical and electrochemical processes during the discharge of NALiO2B for various conditions [1, 31]. Continuum models were built to investigate O_2 and Li^+ transport, charge conservation, and electrochemical kinetics during NALiO2B discharge in one dimension. The results showed that the reducing cathode thickness improved the O_2 transport for electrochemical reaction, thus enhancing the specific capacity [32]. By considering electrode exchange at electrode–Li_2O_2–electrolyte interfaces, Liu et al. explained that the maximum NALiO2B capacity was limited by the insufficient O_2 diffusion at high current densities and by the Li_2O_2-induced pore blockages at low current densities [33]. Various 1D simulations were conducted to explore effects of cathode structures. Bi-porous cathodes, containing mesopores for electrochemical reaction and macropores for O_2 reservoir, were shown to sustain the stable electrochemical reaction and improve the NALiO2B performance [34]. Cathode porosity was proven to the key factor affecting NALiO2B capacity and a hierarchical cathodes were suggested to enhance NALiO2B capacity by up to 10.38% [35]. Proper cathode designs (e.g., partially flooded electrodes) were reported to shorten the O_2 diffusion path, improve the reaction process, and optimize the NALiO2B operation [36]. In addition to these 1D studies, Wang et al. built a two-dimensional (2D) model to investigate NALiO2B discharge and indicated that the decreased electrolyte concentration caused sharp drops in discharge capacity [37]. Zhang et al. analyzed the macroscopic discharge behaviors of NALiO2B in two dimensions. They found that electrodes with gradient porosity could enhance O_2 diffusion and battery capacity, but the excessively large

gradient porosity could lead to significant overpotential and deteriorated battery performance [38]. In parallel, some three-dimensional (3D) simulations of NALiO2B were carried out. Gwak and Ju proposed a 3D transient model to investigate NALiO2B discharge, which demonstrated the optimized electrode thickness and electrolyte filling degree were crucial for achieving the continuous reaction process and the high discharge capacity [39]. Meso-scale simulations of NALiO2B discharge revealed that, as the electrode load (or thickness) increased, the effective diffusion coefficient of O_2 continuously decreased. Meanwhile, the specific discharge capacity initially grew significantly, then began to decline slightly after reaching its peak value [40]. Based on the density functional theory, the discharge process of NALiO2B was investigated at microscales. Silicene cathode surfaces with attached hydrophobic functional groups demonstrated excellent discharge performance [41], pillared δ-MnO_2 structures were found to be highly efficient reaction catalysts for NALiO2B [42], and single-layer Tl_2O was identified as a viable catalyst for NALiO2B [43].

These numerical studies have achieved significant breakthroughs in understanding the physical and electrochemical processes during the discharge of NALiO2B, which contributed to the prediction and optimization of NALiO2B [31]. However, due to the porous cathode structure, existing models were constructed at macroscopic scales. Correspondingly, volume-averaged structures and effective parameters were utilized, electrode, electrolyte, and Li_2O_2 were treated as a homogeneous continuum, and the pore-scale details (e.g., nonuniformity and reaction kinetics) were neglected. The overall battery behaviors, which are macroscopic manifestations of micro- and meso-scale phenomena within the cell, are strongly influenced by physical and electrochemical processes at the pore scale. Therefore, a pore-scale study of NALiO2B discharge is urgently needed to elucidate the underlying multiphysics and explain the macroscopic battery performance, which will offer valuable insights to guide the battery design and optimization.

Over the past three decades, the lattice Boltzmann (LB) method has been extensively applied as a powerful pore-scale solver to investigate reactive fluid transport in porous structures [44,45]. Accordingly, LB simulations have been conducted to explore the multiphysics involved in the battery field, including the transport of species and ions, the distribution of multiple phases, the charge conservation, and the electrochemical kinetics [46–50]. LB simulations have been conducted to provide pore-scale insights into flow battery, LiB, and fuel cells. To our best knowledge, however, limited LB models have been specifically developed for NALiO2B because of the intricate morphology of Li_2O_2. Fang et al. proposed an LB model to investigate the reactive transport processes during NALiO2B discharge at the pore scale. They showed that the discharge capacity increased with the cathode porosity but decreased as the current density increases [51]. Although this study offered pore-scale insights into the discharge behaviors of NALiO2B, it still encountered several limitations as follows. First, the proposed model considered O_2 transport in a cathode fully filled by electrolyte, thus neglecting the multiphase distribution of air and electrolyte, the Li^+ transport within the electrolyte, the O_2 concentration jump across the air–electrolyte interface, and the charge distributions. Additionally, the overpotential and the current density generated by electrochemical reaction are estimated using the overall charge conservation, without accounting for local potential or O_2 concentration. Second, the generated Li_2O_2 is simplified as a homogeneous film on cathode surface, ignoring its intricate and heterogeneous morphologies. Third, impacts of the insufficient O_2 diffusion on electrochemical reactions are not discussed. Finally, effects of various electrode structures and electrolyte filling degrees on the transport and reaction dynamics are not investigated, which may impede explanation of experimental observations like battery performance in cathodes with partially infiltrated electrolyte. To overcome these limitations and advance the capability of LB method, this work aims to develop a 3D electrochemical LB model for studying NALiO2B discharge at the pore scale. The objective of this research is to elucidate the electrolyte and air distributions, O_2 and Li^+ transport, complex Li_2O_2 structures, electrochemical kinetics, as well as to evaluate the battery performance under various battery designs and current densities.
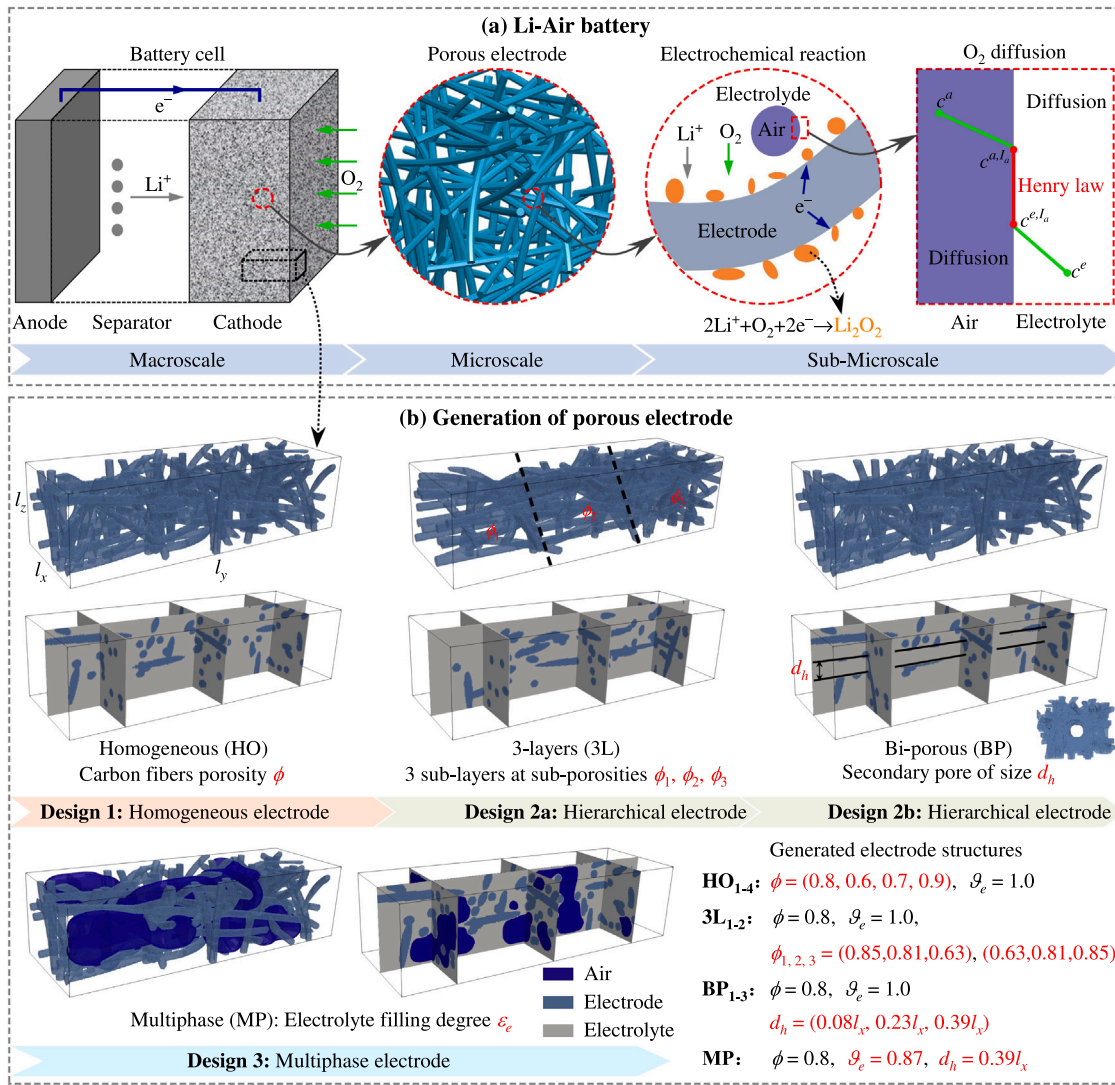
Fig. 1. Schematic descriptions of (a) the NALiO2B configuration and pore-scale physical-electrochemical processes, and (b) the generation of porous electrodes.

2. Methodology

The configuration of an NALiO2B is shown in Fig. 1(a), comprising a Li metal anode, a separator, and a porous air cathode. This work investigates the discharge of NALiO2B in cathode without detailing the physical and electrochemical processes in anode. On the cathode side, the porous electrode structure provides active sites for electrochemical reactions, while void pores within the electrode are filled with electrolyte or air bubbles. The physical-electrochemical processes mainly include the transport of O_2 and Li^+ in the air (gas) and electrolyte (liquid) phases, the electronic conduction in the electrode (solid) phase, and the electrochemical reaction on electrode surfaces. During discharge, O_2 from ambient air dissolves into electrolyte and transports to electrode surfaces, where it reacts with Li^+ to generate Li_2O_2. By ignoring intermediates, the electrochemical reaction in cathode is described by [31],

$$2Li^+ + O_2 + 2e^- \rightarrow Li_2O_2. \tag{1}$$

Resolving all the above processes in a complex 3D microstructure is computationally expensive, and simplifications are applied as follows. (1) The computational domain is reduced to a small-size one that decreases the computational cost while holding the discharge properties of NALiO2B. (2) Li_2O_2 is the only discharge product and it accumulates on electrode surfaces. (3) The tunneling-limited length of electron is 10 nm for Li_2O_2 and the local electrode surface becomes deactivated once the Li_2O_2 layer is thicker than 10 nm. (4) NALiO2B discharges in a galvanostatic and isothermal condition and the internal convection is negligible. (5) The discharge process of NALiO2B and the reverse reaction in Eq. (1) are not considered. (6) The overpotential of the anode reaction is negligible.

2.1. Electrode generation

The cathode structure effectively affects the electrochemical kinetics and the battery performance, thus requiring careful optimizations of its microstructure. This study generates cathode microstructures that encompass porous electrodes, void pores, and multiphase distributions of electrolyte and air. As depicted in Fig. 1(b), a domain of size $l_x \times l_y \times l_z$ is firstly selected from the cathode. Then, carbon fibers at a uniform diameter d are configured in this domain to construct homogeneous porous electrodes (HO). Using this design, 4 electrodes HO_{1-4} are produced to consider different structure porosities ϕ ranging from 0.6 to 0.9. On the other hand, hierarchical electrodes with a given porosity ϕ are designed to feature either three sub-layers or bi-scale pores. Specifically, the three-layer (3L) electrode comprises three sub-layers at sub-porosities ϕ_1, ϕ_2, and ϕ_3, and the bi-porous (BP) electrode features a secondary pore (or a large-size pore) of diameter d_h in the electrode

center. This study examines 2 electrodes $3L_{1-2}$ and 3 electrodes BP_{1-3}. The sub-porosities of $3L_{1-2}$ either increase or decrease along the l_y direction, and the d_h values of BP_{1-3} vary from $0.08l_x$ to $0.39l_x$. In the final design of the multiphase (MP) electrode, the electrolyte is partially infiltrated into the electrode at a filling degree of ϑ_e and air bubbles exist in the electrode. Further details on the generation parameters of electrodes are provided in Fig. 1(b).

2.2. Mathematical model

Under the above premises, governing equations are built to describe the air–electrolyte distributions, transport of Li^+ and O_2, charged conservation, and electrochemical reaction in cathode at the pore scale. The distribution of electrolyte and air is modeled as multiphase flow [44,52],

$$\nabla \cdot (\rho \boldsymbol{u}) = 0, \tag{2}$$

$$\frac{\partial (\rho \boldsymbol{u})}{\partial t} + \nabla \cdot (\rho \boldsymbol{u}\boldsymbol{u}) = -\nabla p + \nabla \cdot \left[\rho \nu \left(\nabla \boldsymbol{u} + \nabla \boldsymbol{u}^T\right)\right] + \boldsymbol{F}, \tag{3}$$

where ρ is the fluid density, t is the time, $\boldsymbol{u}$ is the velocity, p is the pressure, ν is the kinematic viscosity, and $\boldsymbol{F}$ is the surface tension force.

The transport of Li^+ in electrolyte contains the diffusion driven by concentration gradient and the migration caused by electrolytic current as [35,53],

$$\frac{\partial c_l}{\partial t} = \nabla \cdot \left(D_{\text{Li}} \nabla c_l\right) - \nabla \cdot \left(\frac{t_+}{F} \boldsymbol{i}\right). \tag{4}$$

Here c_l is the Li^+ concentration, D_{Li} is the Li^+ diffusion coefficient, t_+ is the transference number of Li^+, F is the Faraday constant, and $\boldsymbol{i}$ is the current density vector in electrolyte.

As depicted in Fig. 1(a), O_2 initially diffuses through air, then it traverses the air–electrolyte interface and experiences a concentration drop in line with Henry's law, and finally it proceeds to diffuse within electrolyte as [46],

$$\frac{\partial c^a}{\partial t} = \nabla \cdot \left(D_{O_2}^a \nabla c^a\right), \tag{5}$$

$$c^{a,I_a} = Hc^{e,I_a}, \tag{6}$$

$$\frac{\partial c^e}{\partial t} = \nabla \cdot \left(D_{O_2}^e \nabla c^e\right). \tag{7}$$

Here c and D_{O_2} are concentration and diffusion coefficient of O_2, with superscripts a, I_a, and e representing the air, air–electrolyte interface, and electrolyte, respectively. H is the Henry constant. The overall O_2 concentration is $c = x_a c^a + (1 - x_a) c^e$, with x_a being the phase fraction of air.

The charge conservation in solid (i.e., electrode and Li_2O_2) and electrolyte phases can be expressed as [53],

$$\nabla \cdot (k_s \nabla \varphi_s) = 0. \tag{8}$$

$$\nabla \cdot \boldsymbol{i} = 0, \quad \boldsymbol{i} = k_e \nabla \varphi_e + k_l \nabla \ln c_l, \tag{9}$$

where k and φ denote the charge transfer coefficient and the local potential value, respectively. Their subscripts s and e correspond to the solid and electrolyte phases. k_l is the coefficient related to Li^+ migration.

The electrochemical reaction Eq. (1) takes place at the active electrolyte–solid interface I_s, where the current density j_c is calculated using the Butler–Volmer equation [53],

$$j_c = nFk_c c_l^2 c \exp\left(\frac{-\beta F\eta}{RT}\right), \quad \text{with} \quad \eta = \varphi_s - \varphi_e - E^0. \tag{10}$$

Here $n = 2$ is the number of electrons transferred, k_c is the rate coefficient, $\beta = 0.5$ is the symmetry factor, R is the universal gas constant, T is the operating temperature, η is the overpotential, and E^0 is

the theoretical equilibrium potential for reaction. The electrochemical reaction is then describe by boundary conditions as [54,55],

$$\boldsymbol{n} \cdot D_{\text{Li}} \nabla c_l^{I_s} = -2\frac{j_c}{2F}, \quad \boldsymbol{n} \cdot D_{O_2} \nabla c^{I_s} = -\frac{j_c}{2F}, \tag{11}$$

$$\boldsymbol{n} \cdot k_e^{I_s} \nabla \varphi_e = j_c, \quad \boldsymbol{n} \cdot k_s^{I_s} \nabla \varphi_s = -j_c, \tag{12}$$

$$\frac{\partial V_s}{\partial t} = \frac{j_c}{2F} a_r M_s. \tag{13}$$

In these boundary conditions, $\boldsymbol{n}$ is the interface normal pointing to the electrolyte, V_s and M_s represent the volume and molecular volume of Li_2O_2, respectively, and a_r is the specific surface area per unit volume.

2.3. Numerical method

The LB method is applied to solve the conservation Eqs. (2)–(9) in three dimensions. LB evolution equations are built as follows [46,56–58],

$$f_i\left(\boldsymbol{x} + \boldsymbol{e}_i\delta_t, \, t + \delta_t\right) - f_i\left(\boldsymbol{x}, \, t\right) = -\left(\boldsymbol{M}^{-1}\boldsymbol{S}\boldsymbol{M}\right)_{ij}\left[f_j\left(\boldsymbol{x}, \, t\right) - f_j^{eq}\left(\boldsymbol{x}, \, t\right)\right]$$
$$+ \delta_t\left(\boldsymbol{M}^{-1}\left(\boldsymbol{I} - 0.5\boldsymbol{S}\right)\boldsymbol{M}\right)_{ij} F_j, \tag{14}$$

$$gl_i\left(\boldsymbol{x} + \boldsymbol{e}_i\delta_t, \, t + \delta_t\right) - gl_i\left(\boldsymbol{x}, \, t\right) = -\left(\boldsymbol{M}_l^{-1}\boldsymbol{S}_l\boldsymbol{M}_l\right)_{ij}\left[gl_j\left(\boldsymbol{x}, \, t\right) - gl_j^{eq}\left(\boldsymbol{x}, \, t\right)\right]$$
$$+ \delta_t\left(\boldsymbol{M}_l^{-1}\boldsymbol{S}_l\boldsymbol{M}_l\right)_{ij} F_{l,j}, \tag{15}$$

$$go_i\left(\boldsymbol{x} + \boldsymbol{e}_i\delta_t, \, t + \delta_t\right) - go_i\left(\boldsymbol{x}, \, t\right) =$$
$$-\left(\boldsymbol{M}_o^{-1}\boldsymbol{S}_o\boldsymbol{M}_o\right)_{ij}\left[go_j\left(\boldsymbol{x}, \, t\right) - go_j^{eq}\left(\boldsymbol{x}, \, t\right)\right], \tag{16}$$

$$hs_i\left(\boldsymbol{x} + \boldsymbol{e}_i\delta_t, \, t + \delta_t\right) - hs_i\left(\boldsymbol{x}, \, t\right) =$$
$$-\left(\boldsymbol{M}_s^{-1}\boldsymbol{S}_s\boldsymbol{M}_s\right)_{ij}\left[hs_j\left(\boldsymbol{x}, \, t\right) - hs_j^{eq}\left(\boldsymbol{x}, \, t\right)\right], \tag{17}$$

$$he_i\left(\boldsymbol{x} + \boldsymbol{e}_i\delta_t, \, t + \delta_t\right) - he_i\left(\boldsymbol{x}, \, t\right) =$$
$$-\left(\boldsymbol{M}_e^{-1}\boldsymbol{S}_e\boldsymbol{M}_e\right)_{ij}\left[he_j\left(\boldsymbol{x}, \, t\right) - he_j^{eq}\left(\boldsymbol{x}, \, t\right)\right] + \delta_t\left(\boldsymbol{M}_e^{-1}\boldsymbol{S}_e\boldsymbol{M}_e\right)_{ij} F_{e,j}, \tag{18}$$

where i and j are discrete directions. For particles moving with discrete velocity $\boldsymbol{e}_i$ at position $\boldsymbol{x}$ and time t, $f_i(\boldsymbol{x}, \, t)$, $gl_i(\boldsymbol{x},t)$, $go_i(\boldsymbol{x},t)$, $hs_i(\boldsymbol{x},t)$, and $he_i(\boldsymbol{x},t)$ are distribution functions of the hydrodynamic, Li^+ and O_2 concentrations, and potential values in solid and electrolyte, respectively. The superscript eq indicates their equilibrium distribution functions. F_j, $F_{l,j}$, and $F_{e,j}$ are distribution functions for source terms. $\boldsymbol{S}$, $\boldsymbol{S}_l$, $\boldsymbol{S}_o$, $\boldsymbol{S}_s$, and $\boldsymbol{S}_e$ are the diagonal relaxation matrices, whereas $\boldsymbol{M}$, $\boldsymbol{M}_l$, $\boldsymbol{M}_o$, $\boldsymbol{M}_s$, and $\boldsymbol{M}_e$ are transformation matrices to map distribution functions from the physical space to the moment space. At each time step, after the above evolutions, the macroscopic variables are calculated as,

$$\rho = \sum_i f_i, \quad \rho\boldsymbol{u} = \sum_i \boldsymbol{e}_i f_i + \frac{\delta_t \boldsymbol{F}}{2}, \quad c_l = \sum_i gl_i, \quad c = \sum_i go_i,$$
$$\varphi_s = \sum_i hs_i, \quad \varphi_e = \sum_i he_i. \tag{19}$$

To enforce boundary conditions for the electrochemical reaction at electrolyte–solid interfaces and the O_2 transport across air–electrolyte interfaces, LB boundary schemes are developed. More details are provided in Appendix B.

3. Results and discussion

Based on the generated 3D electrodes, pore-scale simulations are conducted to study the discharge performance of NALiO2B. As illustrated in Fig. 2(a), from the domain inlet ($y = 0$), the incompressible air containing O_2 at an initial concentration c_0 diffuses in and a fixed current density I_0 is implemented. On the opposite side ($y = l_y$), Li^+ at an initial concentration $c_{1,0}$ diffuses to react with O_2 and generate Li_2O_2 on

Table 1
Physical properties for simulations of NALiO2B discharge.

Parameters	Symbol	Values
Domain size	$l_x \times l_y \times l_z$	0.64 μm × 1.92 μm × 0.5 μm
Grid size	$N_x \times N_y \times N_z$	128 × 384 × 100, 5 nm/grid
Carbon fibers diameter	d	0.05 μm
Hole diameter	d_h	(0.05, 0.15, 0.25) μm
Ambient O_2 concentration	c_0	9.46 mol/m³
Initial Li^+ concentration	$c_{1,0}$	100 mol/m³
Henry constant	H	4.5
O_2 diffusion coefficient in air	$D_{O_2}^a$	1.81×10^{-5} m²/s
O_2 diffusion coefficient in electrolyte	$D_{O_2}^e$	2.2×10^{-10} m²/s
Li^+ diffusion coefficient	D_{Li}	3.0×10^{-11} m²/s
Faraday constant	F	96 485.34 C/mol
Theoretical equilibrium potential	E^0	2.96 V
Operating temperature	T	300 K
Universal gas constant	R	8.314 J/mol K
Current density	I_0	(2.5, 5, 7.5, 10, 15, 25) A/m²
Charge transfer coefficient in electrolyte	k_e	0.552 S/m
Charge transfer coefficient in solid	k_s	212 S/m
Charge transfer coefficient by Li^+	k_l	0.1 S/m
Electrochemical reaction rate coefficient	k_c	3.63×10^{-16} m⁷/mol²s
Li_2O_2 molecular volume	M_s	0.021 L/mol

electrode surfaces. The electrochemical and physical properties used in the following simulations are summarized in Table 1 [39,53,59]. Model validations and grid convergence tests are provided in Appendix C–D. In this study, each simulation test continues until the cell voltage $E_c = \varphi_s - \varphi_e$ drops below the discharge cutoff voltage of 2.0 V. At this battery death point, the depth of discharge (DoD) and the discharge capacity (Q_1, normalized by the electrode mass) are recorded as DoD_m and $Q_{1,m}$, respectively.

3.1. Discharge performance of NALiO2B

The initial objective is to investigate the discharge performance of NALiO2B with the homogeneous electrode HO_1 at a current density $I_0 = 2.5$ A/m². Fig. 2(b) provides microscopic evolutions of Li_2O_2 distributions on electrode surfaces at different DoDs. At DoD = 0.08, Li_2O_2 particles are generated from the O_2 diffusion side ($y = 0$), which is driven by the electrochemical reaction (Eq. (1)) occurring on electrode surfaces. As discharge (or reaction) continues, these Li_2O_2 particles gradually grow to be interconnected and eventually form a layer of irregular Li_2O_2 on the electrode. From DoD = 0.08 to 0.78, such a Li_2O_2 layer moves upwards and expands its coverage on electrode surfaces. This finally results in the part of electrode surfaces near the air inlet being completely covered by Li_2O_2. These Li_2O_2 evolution properties generally align with previous experimental observations [24,60]. In addition, through the zoom-in views in Fig. 2(b), the part of electrode surfaces near the Li^+ inlet is incompletely coated with Li_2O_2 at the battery death point $DoD_m = 0.78$, hence the incomplete discharge of NALiO2B in this case.

Quantitative detection of NALiO2B discharge performance is obtained by recording the Li_2O_2 coverage ratio ε_s, the discharge capacity Q_1, the cell voltage E_c, and the depth of discharge DoD in Fig. 2(c)–(e). Here ε_s is defined as $\varepsilon_s(y) = A_{Li_2O_2}(y)/A_0(y)$, where $A_{Li_2O_2}(y)$ denotes the electrode surfaces covered by Li_2O_2 in the xz-plane at position y, and $A_0(y)$ represents the initial electrode surface area within the same plane. Correspondingly, $\varepsilon_s = 1$ indicates the fully coated electrode with Li_2O_2, $\varepsilon_s = 0$ denotes a clean electrode, and $0 < \varepsilon_s < 1$ stands for the partially coated electrode at position y. Analyzing curves of ε_s in Fig. 2(c), it is observed that as NALiO2B discharges (or DoD increases), ε_s gradually approaches 1, reflecting an enlarged Li_2O_2 coverage ratio

on the electrode. At $DoD_m = 0.78$, a part of the electrode ($y < 0.45l_y$) is entirely covered by Li_2O_2 with $\varepsilon_s = 1$. However, the remaining part ($y > 0.45l_y$) shows $\varepsilon_s < 1$ and is incompletely coated with Li_2O_2. This suggests that NALiO2B undergoes incomplete discharge and it fails to achieve the nominal capacity at the death point DoD_m.

Fig. 2(d) shows that the simulated cell voltage E_c remains at 2.67 V during discharge, before sharply dropping to 2.0 V at the end of discharge. As explained in experiments, this sharp voltage decline results from the decrease in electrochemical surface area [22]. Specifically, the reactive electrode surfaces should be partially or entirely uncovered by Li_2O_2 and simultaneously should be enriched with O_2 to facilitate the electrochemical reaction. However, as Li_2O_2 accumulates on the electrode and O_2 is depleted, the active electrolyte–solid interface I_s diminishes. According to charge conservation, the equation $I_0 A_s = j_c A_r$ should be satisfied, where A_s is the area for imposing I_0 and A_r is the area of I_s. Given that I_0 and A_s remain nearly constant during the discharge of NALiO2B, the decreased A_r requires a larger j_c (or more intense reaction) to sustain the imposed I_0. According to Eq. (10), a larger j_c requires a more negative η (or a higher overpotential) at the given O_2 supply. This finally causes $E_c = E^0 + \eta$ to quickly drop below 2.0 V. From Fig. 2(e), it is observed that the discharge capacity Q_1 increases with DoD and reaches a peak of $Q_{1,m} = 1836.7$ mAh/g at $DoD_m = 0.78$. Given that $DoD_m < 1$, NALiO2B is not fully discharged and $Q_{1,m}$ does not reach the nominal value, supporting Li_2O_2 distributions in Fig. 2(b).

To investigate the cause for the declined reactive electrode surface area A_r and the premature death of NALiO2B, evolutions of the residual electrode surface ratio $\varepsilon_e(y) = 1 - \varepsilon_s(y)$ and the xz-plane averaged O_2 concentration $c_a(y)$ are tracked against Q_1 during discharge, as shown in Fig. 2(f). The findings reveal that at DoD_m (indicated by blue lines), the residual electrode surface area remains available ($\varepsilon_e > 0$) but O_2 is nearly exhausted ($c_a \approx 0$) in the region of $y > 0.45l_y$. For illustration, distributions of the electrode surface area and O_2 concentration at DoD_m are depicted in Fig. 2(g). As can be seen, although there are sufficient electrode surfaces available for electrochemical reaction, these surfaces are not enriched with O_2, resulting in a lack of A_r. It is thus confirms that the limited O_2 diffusion within the electrode is responsible for the suppressed electrochemical reaction area and the premature battery death in this case. To optimize the discharge of NALiO2B, the following sections will focus on rational battery designs to enhance O_2 diffusion within the electrode.

3.2. Design 1: electrode porosity

The first optimization strategy is to change the electrode porosity ϕ. Homogeneous electrodes HO_{1-4}, featuring porosities from 0.6 to 0.9, are constructed. Additional structural parameters are provided in Fig. 1(b). Based on these electrodes, the discharge of NALiO2B is simulated under a current density $I_0 = 2.5$ A/m². The discharge performance is quantitatively evaluated by monitoring the discharge capacities Q_1 and Q_2, the cell voltage E_c, and the depth of discharge DoD as shown in Fig. 3(a)–(b). It is noted that, due to variations in porosity among electrodes HO_{1-4}, the electrode mass m_e differs and the absolute discharge capacity is introduced as $Q_2 = Q_1 m_e$. The profiles in Fig. 3(a)–(b) demonstrate that the discharge performance of NALiO2B shows a similar trend for each tested ϕ. Specifically, during discharge, E_c remains constant at 2.67 V before sharply falling to 2 V, and both Q_1 and Q_2 continue to rise as DoD increases. Alongside these similarities, with the growing ϕ, both DoD and Q_1 increase significantly and the case of $\phi = 0.9$ nearly reaches the nominal discharge capacity with $DoD_m = 0.97$. This suggests that the large ϕ enhances the discharge degree of NALiO2B. However, Q_2 changes non-monotonically with ϕ, displaying a peak value at around $\phi = 0.8$. This stems from the fact that the growing ϕ brings about the diminished m_e and the augmented Q_1. Once the growth in Q_1 is unable to compensate the decline in m_e, the value of $Q_2 = Q_1 m_e$ starts to decrease as ϕ continues to increase.
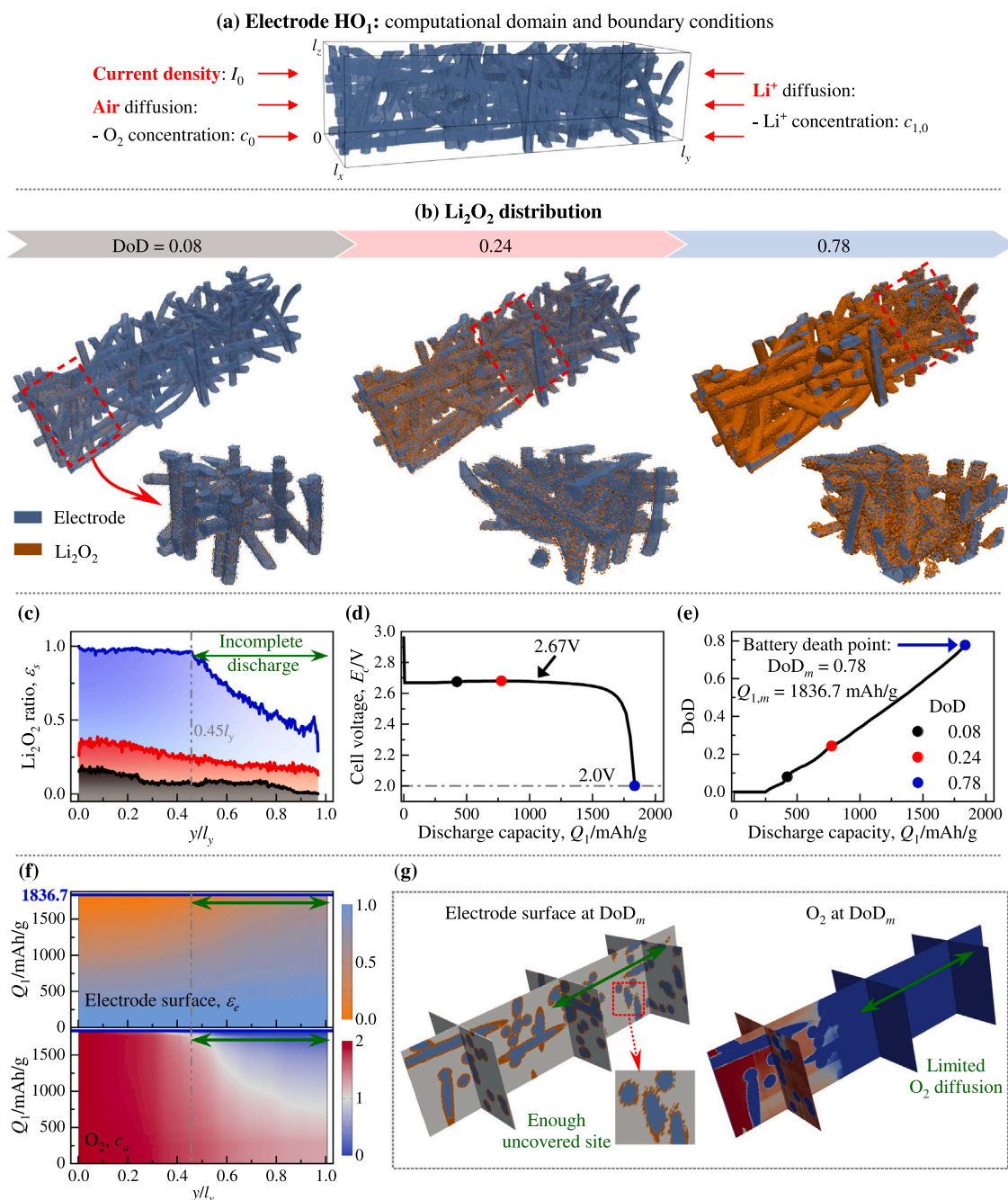
Fig. 2. Discharge of NALiO2B in the electrode HO$_1$ with $I_0 = 2.5$ A/m^2. (a) Electrode structure. (b) Li$_2$O$_2$ structures at DoD = 0.08, 0.25, 0.78. (c) Li$_2$O$_2$ coverage ratio ε_s along the y direction. The discharge capacity Q_1 versus (d) the cell voltage E_c and (e) the depth of discharge DoD. (f) Evolutions of the residual electrode surface ratio ε_e and averaged O$_2$ concentration c_a during discharge. (g) Electrode surface area and O$_2$ concentration distributions at DoD$_m$.

To explore the mechanisms behind the enhancing effect of ϕ on the NALiO2B discharge depth, Fig. 3(c)–(d) display distributions of Li$_2$O$_2$ and O$_2$ at DoD$_m$ for various ϕ values. It is observed that, as ϕ increases, the pore spaces within the electrode expand and the diffusion of O$_2$ is strengthened. This improvement in O$_2$ diffusion boosts the reactive electrode surfaces for electrochemical reaction, thereby amplifying the Li$_2$O$_2$ coverage on the electrode and the discharge degree of NALiO2B (or DoD). For example, the battery is almost fully discharged in the case of $\phi = 0.9$ with DoD$_m = 0.97$, whereas over half of the electrode remains uncovered by Li$_2$O$_2$ and a significant under-discharged NALiO2B with DoD$_m = 0.27$ is observed at $\phi = 0.6$.

The discharge performance of NALiO2B is evaluated by summarizing DoD$_m$, $Q_{1,m}$, and $Q_{2,m}$ across different values of ϕ in Fig. 3(e).

As previously discussed, the case of $\phi = 0.9$ achieves a notably high discharge depth with DoD$_m = 0.97$ and $Q_{1,m} = 2472$ mAh/g. However, in this scenario, $Q_{2,m} = 194$ mAh is comparatively low. For cases of $\phi = 0.6$ and 0.7, the discharge performance is poor across all metrics, with DoD$_m$, $Q_{1,m}$, and $Q_{2,m}$ all showing suboptimal values. Conversely, in the case of $\phi = 0.8$, DoD$_m = 0.78$, $Q_{1,m} = 1837$ mAh/g, and $Q_{2,m} = 289$ mAh are generally satisfactory. When comparing cases of $\phi = 0.9$ and 0.8, it is evident that the $\phi = 0.9$ case is nearly at its nominal capacity and has limited potential for further enhancements. In contrast, the $\phi = 0.8$ scenario, with DoD$_m = 0.78$, shows promise for improvements. Therefore, the electrode structure at $\phi = 0.8$ is considered desirable, and additional battery optimizations are explored in the following sections.
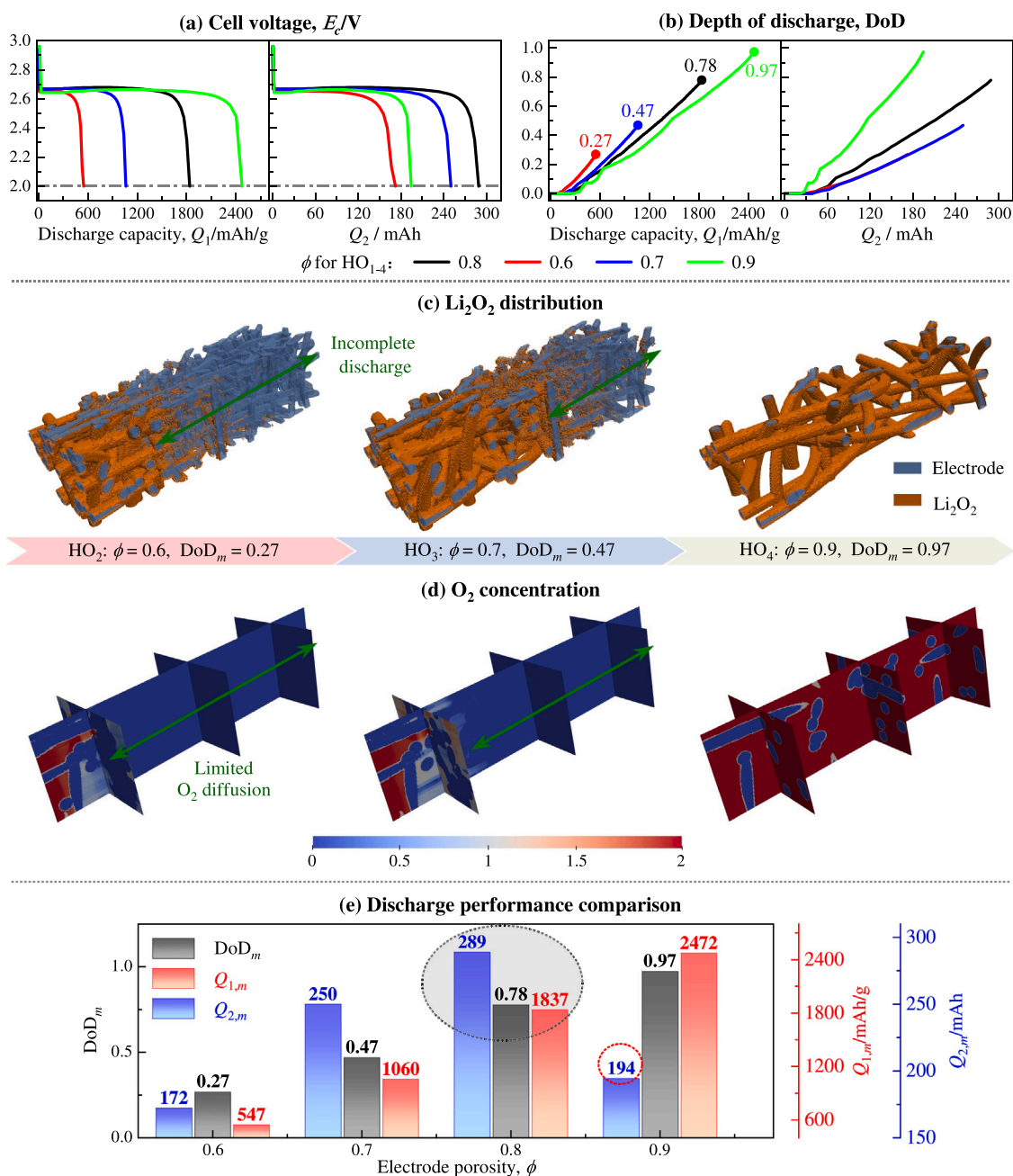
Fig. 3. Discharge of NALiO2B in electrodes HO_{1-4} with $I_0 = 2.5$ A/m^2. (a) The cell voltage E_c versus the specific discharge capacity Q_1 and the absolute discharge capacity Q_2. (b) The depth of discharge DoD versus Q_1 and Q_2. (c) Li_2O_2 and (d) O_2 distributions at DoD_m. (e) The electrode porosity ϕ versus DoD_m, $Q_{1,m}$, and $Q_{2,m}$.

3.3. Design 2: electrode structure

To enhance the NALiO2B discharge performance, hierarchical electrode structures featuring three sub-layers $3L_{1-2}$ and bi-pores BP_{1-3}, have been developed. The specific parameters for these structures are detailed in Fig. 4. The discharge of NALiO2B is simulated at $I_0 = 2.5$ A/m^2 for each electrode structure. The discharge properties, including discharge capacity Q_1, cell voltage E_c, and depth of discharge DoD are depicted in Fig. 4(a)–(b). Similar discharge characteristics are observed across all electrode structures. However, compared to the homogeneous electrode HO_1, hierarchical electrodes demonstrate the ability to improve the discharge depth. Notably, electrodes $3L_1$ and BP_{2-3} significantly enhance the discharge degree, achieving a DoD_m of 0.97. This is corroborated by the Li_2O_2 distributions at DoD_m in Fig. 4(c), where the electrode surfaces of these three structures are almost entirely

covered by Li_2O_2. The discharge performance of NALiO2B is quantitatively compared across different electrode structures in Fig. 4(d). Clearly, when combining DoD_m and $Q_{1,m}$, BP_2 emerges as the most favorable electrode structure because it optimizes NALiO2B to its nominal discharge capacity.

The electrode BP_2 has been demonstrated to be capable of optimizing the battery capacity at a current density of $I_0 = 2.5$ A/m^2. This section further evaluates the rate capability of NALiO2B in the electrode BP_2. For this purpose, the discharge of NALiO2B in BP_2 is simulated for current densities of $I_0 = 2.5, 5, 7.5, 10, 15, 25$ A/m^2. The obtained discharge capacity Q_1, cell voltage E_c, and depth of discharge DoD are illustrated in Fig. 5(b)–(c).

The curves in Fig. 5(b) demonstrate that as I_0 increases, there is a marked decrease in E_c, such as a reduction from 2.67 V at 2.5 A/m^2 to 2.18 V at 25 A/m^2. This trend aligns with previous experimental
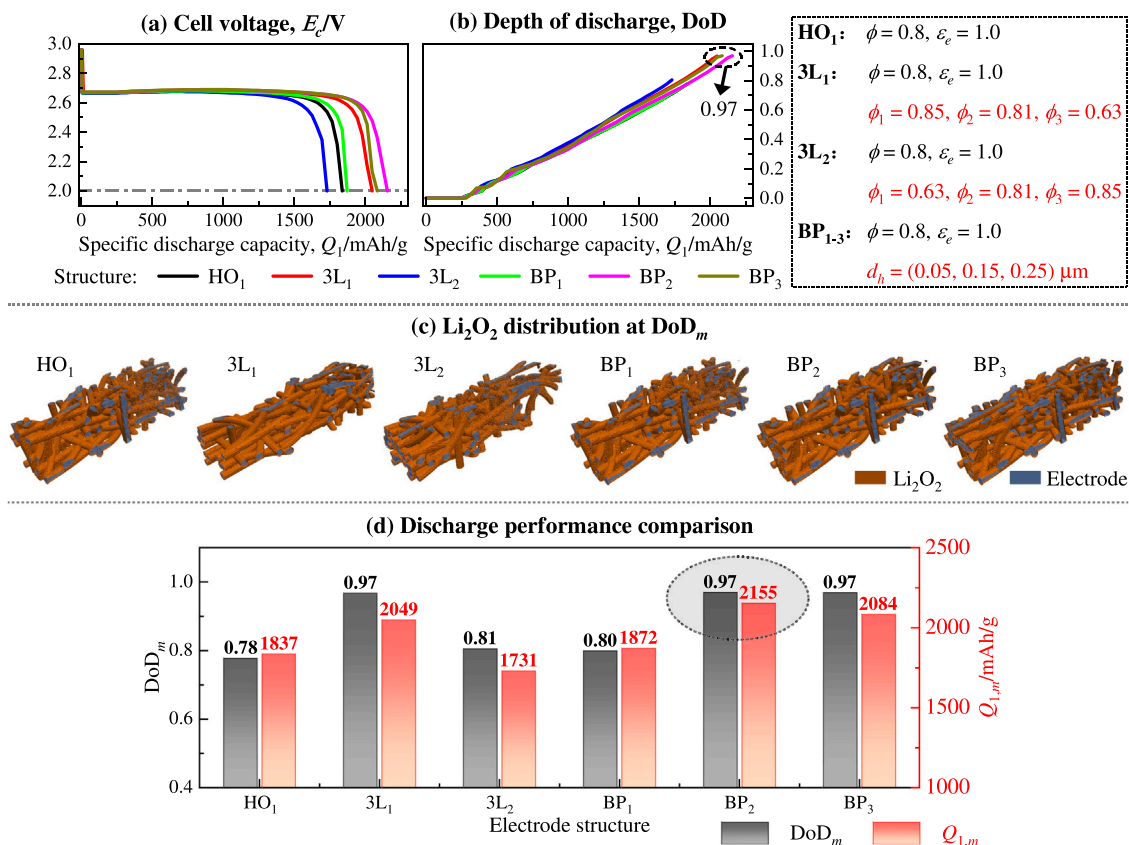
Fig. 4. Discharge of NALiO2B in electrodes HO_1, $3L_{1-2}$, and BP_{1-3} with $I_0 = 2.5$ A/m². The specific discharge capacity Q_1 versus (a) the cell voltage E_c and (b) the depth of discharge DoD. (c) Li₂O₂ distributions at DoD_m. (d) The electrode structures versus DoD_m and $Q_{1,m}$.

findings [61]. It can be explained by the charge conservation equation, $I_0 A_s = j_c A_r$. At the start of discharge, A_s and A_r keep almost constant. The ascending I_0 boosts the value of j_c (or electrochemical reaction) and causes the decreasing η and E_c. Additionally, under high-I_0 conditions, the decline in E_c happens more rapidly and the premature battery death is exacerbated. The relationship of DoD against Q_1 in Fig. 5(c) further supports that the increasing I_0 results in a significant reduction in the discharge performance of NALiO2B. For instance, a DoD_m of 0.97 at 2.5 A/m² falls to 0.36 at 25 A/m².

A bar graph comparing $Q_{1,m}$ and DoD_m for different current densities are provided in Fig. 5(d). A clear trend of degraded discharge performance with the growing I_0 is observed, specifically a decrease of 67.2% in $Q_{1,m}$ from 2.5 to 25 A/m². This reflects the challenges for BP_2 in maintaining the high discharge rates without significant performance losses, hence the poor rate capability of NALiO2B with BP_2. For illustration, Fig. 5(e)–(f) depict the generated Li₂O₂ distributions at DoD_m across various I_0. The results demonstrate the nearly complete coverage of Li₂O₂ on the electrode at a low I_0 of 2.5 A/m². The Li₂O₂ coverage decreases sharply as I_0 increases, and only less than half of the electrode is coated with Li₂O₂ at 25 A/m². This confirms that a large I_0 hinders the complete Li₂O₂ coverage of the electrode and degrades the discharge of NALiO2B.

To understand the rapid premature battery death at high I_0 levels, Fig. 5(g) tracks evolutions of the residual electrode surface ratio ε_e and the averaged O₂ concentration c_a during the discharge process for varying I_0 values. It is evident that, under high-I_0 conditions, the Li₂O₂-uncovered electrode surfaces are adequate but the O₂ availability is restricted. This can be easily understood as a high I_0 boosts the electrochemical reaction (or j_c), thereby accelerating the consumption of O₂. Consequently, the limited O₂ diffusion within the electrode fails to support the intense electrochemical reaction, thus becoming the key factor for the rapid NALiO2B death under large I_0 conditions. In

conclusion, Fig. 5 highlights the low rate capability of NALiO2B with BP_2, calling for optimization strategies to intensify O₂ diffusion within the electrode to support the rapid electrochemical reaction and thereby improve the rate capability of NALiO2B.

3.4. Design 3: electrolyte distributions

To enhance the rate capability of NALiO2B, electrode BP_2 has been expanded to generate a new electrode MP. As illustrated in Fig. 6(a), the electrolyte is partially infiltrated into MP at an filling degree of ϑ_e, and air bubbles within MP act as O₂ reservoirs. Detailed generation parameters for MP can be found in Fig. 1(b). The discharge of NALiO2B in this new electrode MP is simulated across different current densities $I_0 = 2.5, 5, 7.5, 10, 15, 25$ A/m², and the key discharge characteristics are presented in Fig. 6.

Fig. 6(b)–(c) plot the discharge capacity Q_1 against the cell voltage E_c and the depth of discharge DoD for various I_0 values. Similar to the case of BP_2 in Fig. 5, as I_0 increases from 2.5 to 25 A/m², there is a noticeable decrease in both the cell voltage E_c and the maximum discharge degree (or DoD_m). As explained above, this is because a rising I_0 speeds up the electrochemical rate (or O₂ consumption), exacerbates the premature battery death, and degrades the discharge capacity. However, in contrast to BP_2, the degradation impact of increasing I_0 is mitigated in MP, and NALiO2B maintains a satisfactory discharge process. For example, the value of DoD_m for electrode MP remains above 0.7 even at 25 A/m². Quantitative comparisons of NALiO2B discharge performance (i.e., DoD_m and $Q_{1,m}$) between electrodes MP and BP_2 are conducted across different I_0 values in Fig. 6(d)–(e). As can be seen, the electrode MP consistently sustains the discharge capacity and discharge depth at satisfactory levels for all tested I_0 values, verifying results in Fig. 6(b)–(c). Moreover, MP outperforms BP_2 at every I_0, with the performance gap widening significantly as
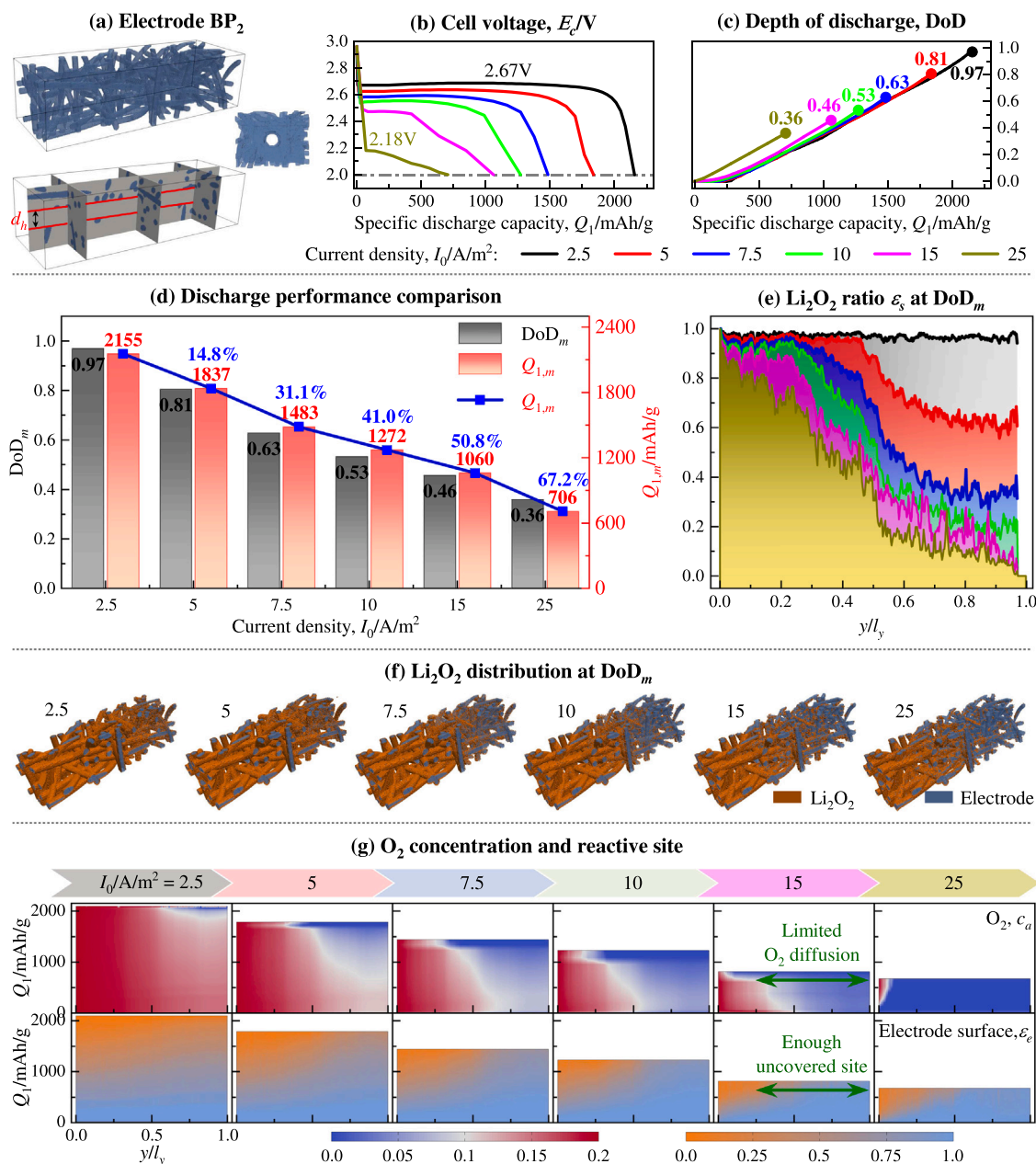
Fig. 5. Discharge of NALiO2B in the electrode BP_2 with I_0 = 2.5, 5, 7.5, 10, 15, 25 A/m². (a) The electrode structure. The specific discharge capacity Q_1 versus (b) the cell voltage E_c and (c) the depth of discharge DoD. (d) Comparison of discharge performance in BP_2 for different I_0 levels. (e)–(f) Li_2O_2 distributions at DoD_m. (g) Evolutions of the residual electrode surface ratio ε_e and averaged O_2 concentration c_a during discharge for different I_0 levels.

I_0 increases. For instance, $Q_{1,m}$ is 95.2% higher in MP than that in BP_2 at 25 A/m², highlighting the superior capacity and rate capability of NALiO2B with MP.

To explore the mechanisms behind the optimized performance of NALiO2B with MP, Fig. 6(f)–(g) visualize the simulated Li_2O_2 and O_2 distributions within electrodes MP and BP_2 at DoD_m and 25 A/m². In the case of MP, most of electrode surfaces is covered by Li_2O_2 and the electrode is enriched with O_2. In contrast, the electrode BP_2 is only sparsely covered by Li_2O_2 and exhibits a significant lack of O_2 around its surfaces. A close observation of the pore-scale O_2 distributions shows that these differences between MP and BP_2 arise from the presence of air bubbles in MP. Considering that the O_2 concentration and diffusion coefficients in air are significantly higher than those in the electrolyte, air bubbles within MP serve as effective O_2 reservoirs. These O_2 reservoirs can significantly enhance O_2 diffusion and increase O_2 availability within MP. Such improvements finally support the rapid

O_2 consumption during the intensified electrochemical reaction under high-I_0 conditions, thereby optimizing the rate capability of NALiO2B.

Overall, these simulation results emphasize the importance of optimized electrode and electrolyte designs in improving NALiO2B discharge performance, particularly under high current densities. The optimized electrode structure BP_2 is found to improve the diffusion of O_2 in electrode, support the continuous electrochemical reaction, and thus boost the discharge capacity of NALiO2B at low current densities. Under high-I_0 conditions however, BP_2 fails to supply the rapid and extensive O_2 consumption driven by the accelerated electrochemical reaction. Therefore, an optimized electrode MP is further proposed that incorporates the partially infiltrated electrolyte and introduces air bubbles to serve as O_2 reservoirs. This design demonstrates the superior capability in handling high I_0 rates and enhancing the rate capability of NALiO2B, which is attributed to the efficient O_2 supply for sustaining the intense electrochemical reaction. These pore-scale results
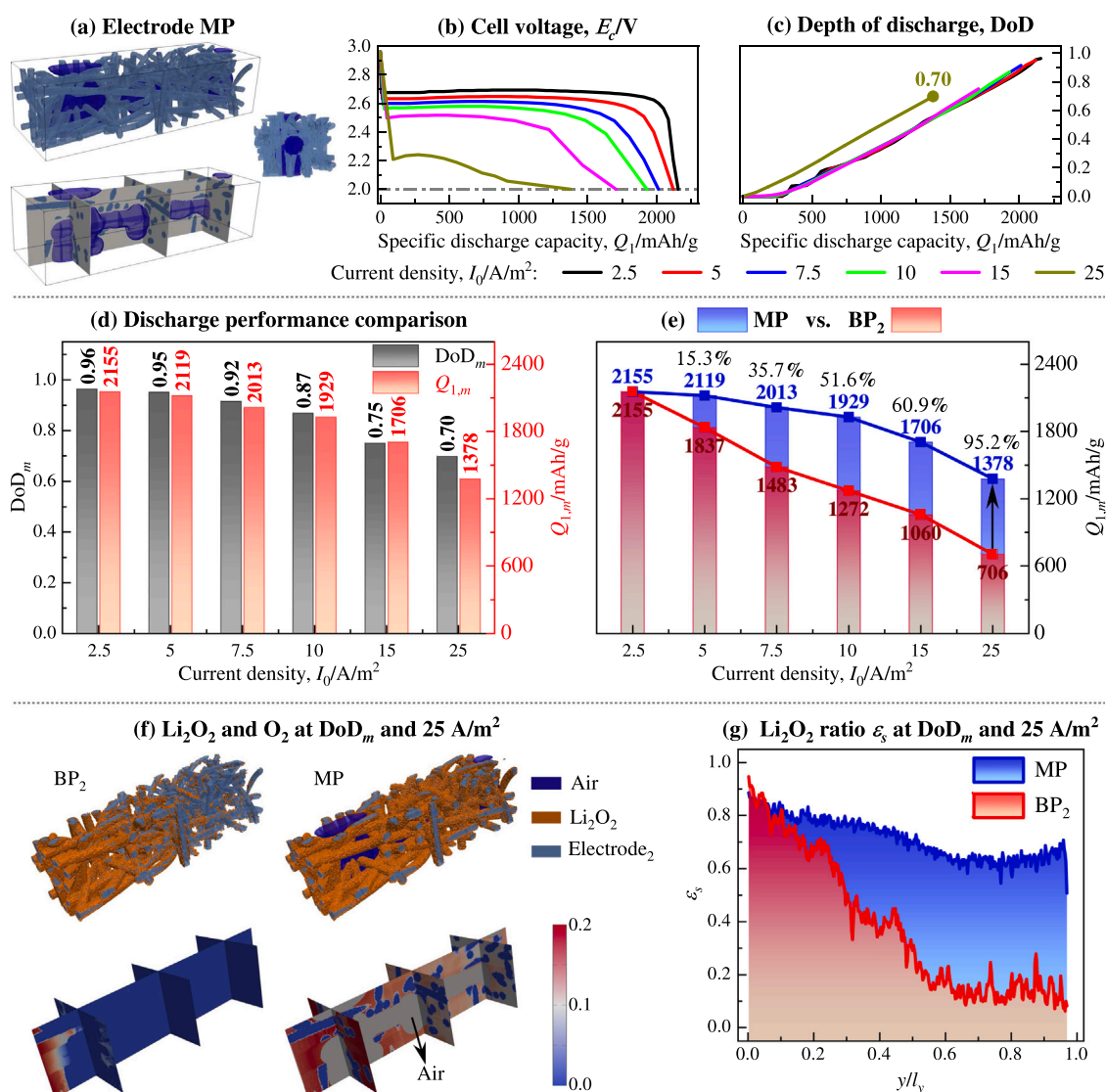
Fig. 6. Discharge of NALiO2B in MP with $I_0 = 2.5, 5, 7.5, 10, 15, 25$ A/m^2. (a) The electrode structure. The specific discharge capacity Q_1 versus (b) the cell voltage E_c and (c) the depth of discharge DoD. (d) Comparison of discharge performance in BP$_2$ for different I_0 levels. (e) Comparison of discharge performance between MP and BP$_2$ for different I_0 levels. (f)–(g) Comparison of Li$_2$O$_2$ and O$_2$ distributions between MP and BP$_2$ at DoD$_m$ and 25 A/m^2.

provide insights into the physical and electrochemical mechanisms underlying NALiO2B discharge, which is critical for high-performance battery technology.

4. Conclusions

In this work, a three-dimensional electrochemical lattice Boltzmann model has been developed for simulating the physical and electrochemical processes during the discharge of NALiO2B. By conducting pore-scale simulations, the discharge capacity and rate capability of NALiO2B are investigated for various electrode and electrolyte designs. During discharge of NALiO2B in a homogeneous electrode HO, the spacial and temporal evolutions of Li$_2$O$_2$, O$_2$, and reactive electrode surface are visualized. The key discharge metrics (i.e., discharge capacity, depth of discharge, and cell voltage) are also analyzed, showing the incomplete discharge of NALiO2B in HO. This premature battery death is mainly due to the restrictive O$_2$ diffusion within the electrode, which reduces the reactive electrode surface area and boosts the electrochemical reaction (or overpotential).

To address this issue, hierarchical electrodes featuring 3-layer or bi-porous designs are constructed. Simulations reveal that the bi-porous

electrode BP$_2$ with large pores can speed up O$_2$ transport, thereby mitigating the premature battery death and increasing the NALiO2B discharge capacity. However, such an electrode design fails to maintain the discharge capacity at high current densities due to the rapid electrochemical reaction and extensive O$_2$ consumption, highlighting the poor rate capability of NALiO2B. For further optimization, a partially infiltrated electrolyte version of BP$_2$ (i.e., electrode MP) is developed for high-current discharge of NALiO2B. Simulations across varying current densities confirm that the electrode MP is capable of maintaining the discharge degree and battery capacity at satisfactory levels. Air bubbles within MP are found to serve as O$_2$ reservoirs to support the fast electrochemical reaction under high current densities, and thus they are the primary contributor to the improved rate capability of NALiO2B.

This work effectively investigates the physical and electrochemical processes behind NALiO2B discharge at the pore scale. The mechanisms causing low discharge capacity and poor rate capability of NALiO2B have been clarified, and various electrode and electrolyte designs for improving the discharge performance of NALiO2B have been explored. This comprehensive study provides valuable insights to guide the design and optimization of NALiO2B. Note that this study focuses on the

Table A.1
Table of superscripts and subscripts.

Superscripts	Meaning	Subscripts	Meaning
a	Air	a	xy-plane average
e	Electrolyte	e	Electrolyte
eq	Equilibrium	$i, j, \bar{\imath}$	Discrete direction
I_a	Air–electrolyte interface	l, Li	Li^+
$'$	Post-collision	m	Battery death point
		o, O_2	O_2
		O_2^a	O_2 in air
		O_2^e	O_2 in electrolyte
		s	Solid
		0	Initial

discharge process of NALiO2B and thus the complete discharge–charge cycles have not been explored. In future work, the proposed LB model will be extended to incorporate both the physical and electrochemical processes involved in the charging of NALiO2B, enabling a comprehensive analysis of battery performance over multiple cycles. Additionally, for a more realistic evaluation of NALiO2B, our future research will consider air composed of multiple components like CO_2, O_2, and H_2O. The interaction and transport of these components, along with potential parasitic reactions and products, may significantly impact the overall battery performance.

CRediT authorship contribution statement

Timan Lei: Writing – original draft, Visualization, Validation, Software, Methodology, Investigation, Formal analysis, Data curation. **Junyu Yang:** Writing – review & editing, Software, Methodology, Investigation. **Geng Wang:** Writing – review & editing, Software, Methodology, Investigation. **Jin Chen:** Writing – review & editing. **Yinglong He:** Writing – review & editing, Visualization. **Kai H. Luo:** Writing – review & editing, Supervision, Resources, Project administration, Investigation, Funding acquisition, Formal analysis, Conceptualization.

Declaration of competing interest

The authors declare that they have no known competing financial interests or personal relationships that could have appeared to influence the work reported in this paper.

Appendix A. Nomenclature

See Tables A.1–A.3.

Appendix B. Electrochemical LB model

Considering the porous electrode structure, the three-dimensional nineteen-velocity (D3Q19) multiple-relaxation-time (MRT) lattice Boltzmann (LB) method is applied for multiphase flow to avoid the unphysical permeability dependence on viscosity at the pore scale [52, 62]. Meanwhile, the D3Q7 MRT LB model is employed for Li^+ and O_2

transport and for charge transfer, which has been proven to be efficient and reliable for a wide range of scalar transport processes [46].

To implement the electrochemical reaction in Eq. (1) at the active electrolyte–solid interface I_s, the boundary conditions outlined in Eqs. (11)–(13) need to be addressed. First, the mass conservation conditions in Eq. (11) are solved. Using Chapman–Enskog analysis, the unknown distribution functions at the electrolyte grid x_e next to I_s are calculated as [52],

$$gl_{\bar{\imath}}\left(x_e,\ t+\delta_t\right)=gl_i'\left(x_e,\ t\right)-2\frac{j_c}{2F},\quad go_{\bar{\imath}}\left(x_e,\ t+\delta_t\right)=go_i'\left(x_e,\ t\right)-\frac{j_c}{2F}.$$
(B.1)

Here, the superscript $'$ denotes the post-collision distribution function, $\bar{\imath}$ is the opposite direction of i as $e_i=-e_{\bar{\imath}}$, and e_i points to the solid phase zone. Then, the charge conservation conditions in Eq. (12) are implemented. Similarly, the unknown distribution functions at the adjacent electrolyte grid x_e or solid grid x_s are determined by [52],

$$he_{\bar{\imath}}\left(x_e,\ t+\delta_t\right)=he_i'\left(x_e,\ t\right)+j_c,\quad hs_i\left(x_s,\ t+\delta_t\right)=hs_{\bar{\imath}}'\left(x_s,\ t\right)-j_c. \quad \text{(B.2)}$$

The evolution of Li_2O_2 at the pore scale, driven by electrochemical reaction, is monitored using Eq. (13). In LB simulations, this structural evolution is addressed by the commonly used volume of pixel method [54,63]. Specifically, a sufficiently fine mesh is chosen to encompass the computational domain, with each grid node positioned at the center of a control cell sized $1 \times 1 \times 1$ in lattice units. Each grid is assumed to represent a single material: solid electrode, solid Li_2O_2, liquid electrolyte, or air. Initially, the Li_2O_2 volume is set as $V_s = 1$ for Li_2O_2 grids and $V_s = 0$ for all other grids. As the discharge process continues, V_s is recalculated at each time step by,

$$V_s\left(t+\delta_t\right)=V_s(t)+\frac{j_c}{2F}a_rM_s.$$
(B.3)

With the accumulation of Li_2O_2 on electrode surfaces, V_s increases over time. When V_s doubles to 2 at a solid Li_2O_2 grid or reaches 1 at an electrode grid, one of its neighboring electrolyte grids is converted into a solid Li_2O_2 grid. The growth probability ratio between neighboring and diagonal grids aligns with the weight coefficient ratio w_i [54].

Attention is finally focused on addressing O_2 transport across the air–electrolyte interface I_a, where a significant jump in O_2 concentration occurs, as described by Eq. (6) and Fig. 1(a). In the present LB simulations, the following scheme is applied to determine the unknown distribution functions at the electrolyte grid x_e and the air grid x_a, both adjacent to I_a [46],

$$go_{\bar{\imath}}\left(x_e,\ t+\delta_t\right)=-\frac{1}{1/H+1}\left[\left(-\frac{1}{H}+1\right)go_i'\left(x_e,\ t\right)-\frac{2}{H}go_{\bar{\imath}}'\left(x_a,\ t\right)\right],$$
(B.4)

$$go_i\left(x_a,\ t+\delta_t\right)=-\frac{1}{1/H+1}\left[\left(\frac{1}{H}-1\right)go_{\bar{\imath}}'\left(x_a,\ t\right)-2go_i'\left(x_e,\ t\right)\right]. \quad \text{(B.5)}$$

Here e_i points to the air phase zone and $x_a = x_e + e_i\delta_t$.

Appendix C. Model validation

Two validation tests with widely-accepted theoretical or experimental solutions are conducted to assess the reliability of the proposed electrochemical LB model for simulating NALiO2B discharge. The first test examines the discharge performance of a simplified NALiO2B featuring a flat cathode electrode, as shown in Fig. C.1(a). In this setup, the simulation domain is 0.2 μm × 0.15 μm × 0.15 μm with a grid resolution of 2.5 nm [51]. From the left inlet, O_2 and Li^+ diffuse into the domain and transport to the electrode surface, where $I_0 = 2.5$ mA/m^2 is applied. On the electrode surface, the electrochemical reaction in Eq. (1) takes place and produces Li_2O_2. Once the layer of Li_2O_2 reaches the tunneling-limited length for electrons, the electrode becomes insulated and the discharge process comes to the death point.

Table A.2
Table of symbols.

Symbols	Meaning	Symbols	Meaning
$A_{Li_2O_2}$ (m^2)	Electrode surfaces covered by Li$_2$O$_2$	I_0 (A/m^2)	External current density
A_0 (m^2)	Initial electrode surface	I_s	Active electrolyte–solid interface
A_s (m^2)	Area for imposing I_0	i (A/m^2)	Current density vector in electrolyte
A_r (m^2)	Area of I_s	j_c (A/m^2)	Current density at I_s
a_r (1/m)	Specific surface area per volume	k (S/m)	Charge transfer coefficient
c (mol/L)	O$_2$ concentration	k_c (m^7/mol^2 s)	Electrochemical reaction rate
c_l (mol/L)	Li$^+$ concentration	$l_{x, y, z}$ (μm)	Domain size
d (μm)	Carbon fibers diameter	m_e (g)	Electrode mass
d_h (μm)	Hole diameter	M	Transformation matrix
D (m^2/s)	Diffusion coefficient	M_s (L/mol)	Li$_2$O$_2$ molecular volume
E_c (V)	Cell voltage	$N_{x, y, z}$	Grid size
E^0 (V)	Theoretical equilibrium potential	n	Number of electrons transferred
e_i	Discrete velocity	n	Interface normal
F (N/m^3)	Surface tension force	p (N/m^2)	Pressure
F (C/mol)	Faraday constant	Q_1 (mAh/g)	Discharge capacity
F_j	Distribution functions of F	Q_2 (mAh)	Absolute discharge capacity
$F_{l,j}$	Distribution functions of $\nabla \cdot \left(\frac{t_+}{F} i \right)$	R (J/mol K)	Universal gas constant
$F_{e,j}$	Distribution functions of $\nabla^2 \ln c_l$	T (K)	Operating temperature
f_i	Distribution functions of ρ	t (s)	Time
gl_i	Distribution functions of c_l	t_+	Transference number of Li$^+$
go_i	Distribution functions of c_{O_2}	u (m/s)	Velocity
hs_i	Distribution functions of φ_s	V_s	Li$_2$O$_2$ volume per volume
he_i	Distribution functions of φ_e	x (m)	Position
H	Henry constant	x_a	Phase fraction of air
β	Symmetry factor	ρ (kg/m^3)	Density
η (V)	Overpotential	ϑ_e	Electrolyte filling degree
ν (m^2/s)	Kinematic viscosity	φ (V)	Local potential
ϕ	Electrode porosity	ε_s	Li$_2$O$_2$ coverage ratio
ε_e	Residual electrode surface ratio		

Table A.3
Table of abbreviations.

Abbreviation	Meaning
BP	Bi-porous
DoD	Depth of discharge
D3Q19	Three-dimensional nineteen-velocity
D3Q7	Three-dimensional seven-velocity
HO	Homogeneous
LB	Lattice Boltzmann
LiB	Lithium-ion battery
LiO2B	Li–O$_2$ battery
MP	Multiphase
MRT	Multiple-relaxation-time
NALiO2B	Non-aqueous Li–O$_2$ battery
3L	3-layers

The calculated cell voltage E_c plotted against the discharge capacity Q_1 is shown in Fig. C.1(b). As can be seen, the present LB model produces the same discharge performance as that in [51], with the obtained capacity of $Q_{1,m} = 2604.3$ mAh/g closely aligning with the theoretical result of 2604.4 mAh/g.

Subsequently, the LB model is validated by simulating the NALiO2B discharge in an electrode with microstructure, as depicted in Fig. C.1 (c). The calculated discharge performance is compared with experimental results obtained by Lu et al. [53,59], with the same simulation parameters being applied. The comparison of E_c and Q_1 are provided in Fig. C.1(d), revealing a good agreement. Previous experiments measured $Q_1 = 2690$ mAh/g and the present LB model yields $Q_1 = 2679$ mAh/g, resulting in a relative error of only 0.4%. These two validation cases confirm the reliability of the proposed electrochemical LB model for simulating NALiO2B discharge.

Appendix D. Grid convergence test

Grid-independence simulations of NALiO2B discharge are conducted using three different grids: $64 \times 192 \times 50$, $128 \times 384 \times 100$, and $256 \times 768 \times 200$. As an example, simulation results for the electrode HO$_1$ at $I_0 = 2.5$ A/m^2 are presented and analyzed. The simulated Li$_2$O$_2$ distributions are shown in Fig. D.1(a), revealing that all three grid resolutions display similar Li$_2$O$_2$ growth characteristics on electrode surfaces. However, differences between these tests are also evident. The finer grids (i.e., $128 \times 384 \times 100$ and $256 \times 768 \times 200$) can accurately capture the delicate and sparse structures of Li$_2$O$_2$, while the coarser grid (i.e., $64 \times 192 \times 50$) is less effective in representing such intricate Li$_2$O$_2$ structures on the top side of the electrode.

Quantitative comparisons of key discharge metrics, including the cell voltage E_c, discharge capacity Q_1, and depth of discharge DoD are provided in Fig. D.1(b)–(c). The profiles of these metrics exhibit similar trends across all three grids, with results from the $128 \times 384 \times 100$ and $256 \times 768 \times 200$ grids closely aligning. In contrast, the coarse grid $64 \times 192 \times 50$ brings about the slightly lower discharge capacity and the under-predicted performance. This can be explained by the incomplete representation of the Li$_2$O$_2$ structure, as shown in Fig. D.1(a). These comparisons indicate that the $128 \times 384 \times 100$ grid resolution is sufficient for achieving grid-independent results. Thus, this grid size is used for simulations throughout this work.

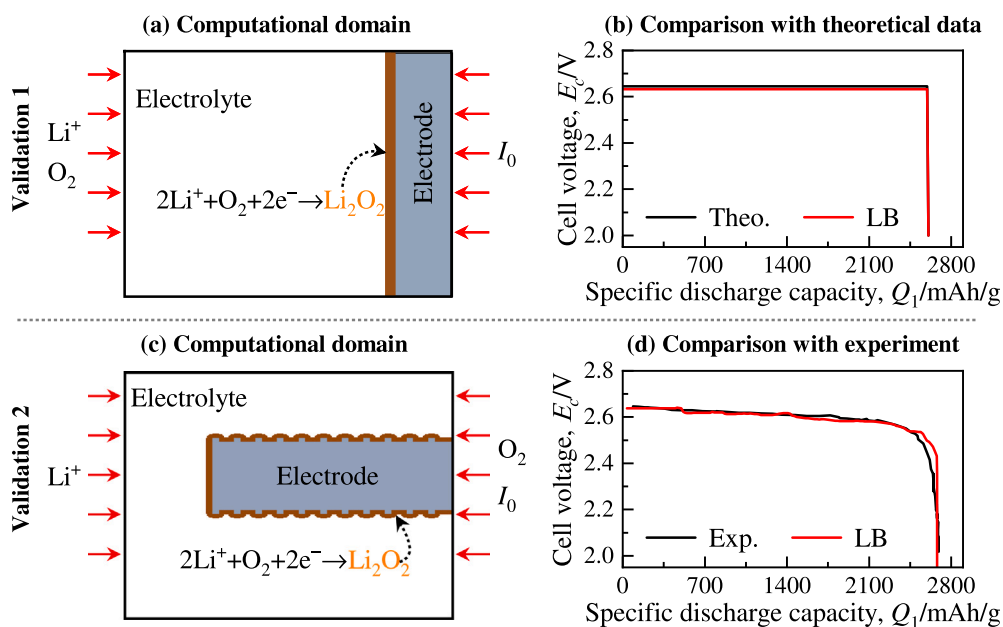## Data availability

Data will be made available on request.

Fig. C.1. Two model validation tests. (a) and (c) Computational domain and boundary conditions. Comparison of discharge performance between numerical results and (b) the theoretical data in [51] and (d) the experimental measurement in [53,59].
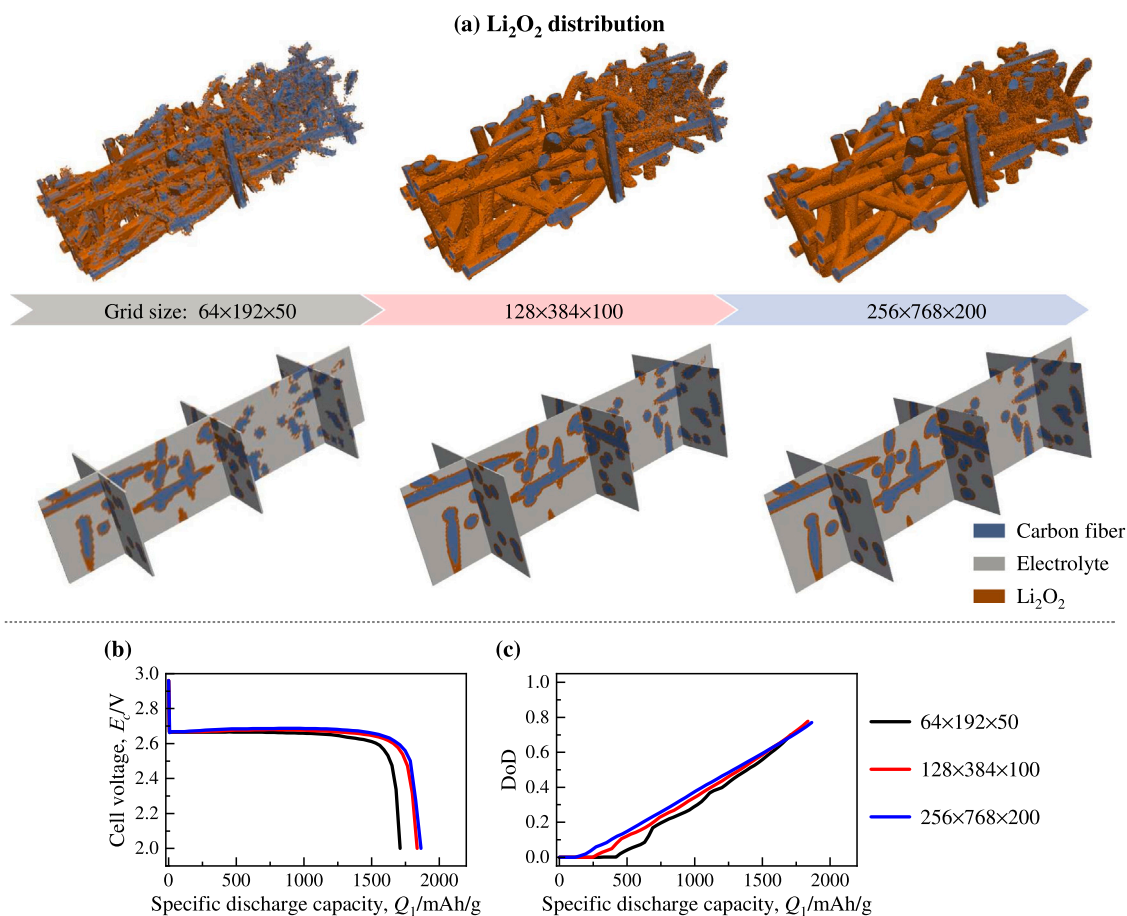

Fig. D.1. Grid convergence test. (a) Li_2O_2 distributions on the electrode HO_1 at DoD_m with three grid resolutions. The specific discharge capacity Q_1 versus (b) the cell voltage E_c and (c) the depth of discharge DoD for three grid resolutions.

References

[1] F. Wang, X. Li, X. Hao, J. Tan, Review and recent advances in mass transfer in positive electrodes of aprotic Li–O₂ batteries, ACS Appl. Energy Mater. 3 (3) (2020) 2258–2270, http://dx.doi.org/10.1021/acsaem.9b02237.

[2] Y. Cao, H. Lu, B. Xu, W. Yang, Q. Hong, Nitrogen/sulfur dual-doped porous carbon nanofibers with Co₉S₈ nanoparticles encapsulated by graphitic shells: a highly active stable free-standing air electrode for rechargeable non-aqueous Li–O₂ batteries and primary alkaline Al-air batteries, Chem. Eng. J. 378 (2019) 122247, http://dx.doi.org/10.1016/j.cej.2019.122247.

[3] W.J. Kwak, Rosy, D. Sharon, C. Xia, H. Kim, L.R. Johnson, P.G. Bruce, L.F. Nazar, Y.K. Sun, A.A. Frimer, M. Noked, S.A. Freunberger, D. Aurbach, Lithium–oxygen batteries and related systems: potential, status, and future, Chem. Rev. 120 (14) (2020) 6626–6683, http://dx.doi.org/10.1021/acs.chemrev.9b00609.

[4] Y. Fu, X. Lei, H. Yin, X. Liu, Rational reconfiguration of a gradient redox mediator with in-situ fabricated gel electrolyte for Li–air batteries, Chem. Eng. J. 416 (2021) 129016, http://dx.doi.org/10.1016/j.cej.2021.129016.

[5] G. Girishkumar, B. McCloskey, A.C. Luntz, S. Swanson, W. Wilcke, Lithium–air battery: promise and challenges, J. Phys. Chem. Lett. 1 (14) (2010) 2193–2203, http://dx.doi.org/10.1021/jz1005384.

[6] K.G. Gallagher, S. Goebel, T. Greszler, M. Mathias, W. Oelerich, D. Eroglu, V. Srinivasan, Quantifying the promise of lithium–air batteries for electric vehicles, Energy Environ. Sci. 7 (5) (2014) 1555–1563, http://dx.doi.org/10.1039/c3ee43870h.

[7] P.G. Bruce, S.A. Freunberger, L.J. Hardwick, J.M. Tarascon, Li–O₂ and Li–S batteries with high energy storage, Nat. Mater. 11 (1) (2012) 19–29, http://dx.doi.org/10.1038/NMAT3191.

[8] H.D. Lim, B. Lee, Y. Bae, H. Park, Y. Ko, H. Kim, J. Kim, K. Kang, Reaction chemistry in rechargeable Li–O₂ batteries, Chem. Soc. Rev. 46 (10) (2017) 2873–2888, http://dx.doi.org/10.1039/c6cs00929h.

[9] Y. Li, Y. Huang, Z. Zhang, D. Duan, X. Hao, S. Liu, Preparation and structural evolution of well aligned-carbon nanotube arrays onto conductive carbon-black layer/carbon paper substrate with enhanced discharge capacity for Li–air batteries, Chem. Eng. J. 283 (2016) 911–921, http://dx.doi.org/10.1016/j.cej.2015.08.063.

[10] K. Abraham, Z. Jiang, A polymer electrolyte-based rechargeable lithium/oxygen battery, J. Electrochem. Soc. 143 (1) (1996) 1, http://dx.doi.org/10.1149/1.1836378.

[11] P. Zhang, M. Ding, X. Li, C. Li, Z. Li, L. Yin, Challenges and strategy on parasitic reaction for high-performance nonaqueous lithium–oxygen batteries, Adv. Energy Mater. 10 (40) (2020) 2001789, http://dx.doi.org/10.1002/aenm.202001789.

[12] K. Hayat, L.F. Vega, A. AlHajaj, What have we learned by multiscale models on improving the cathode storage capacity of li–air batteries? Recent advances and remaining challenges, Renew. Sustain. Energy Rev. 154 (2022) 111849, http://dx.doi.org/10.1016/j.rser.2021.111849.

[13] Z. Zhang, X. Xiao, X. Zhu, P. Tan, Addressing transport issues in non-aqueous Li–air batteries to achieving high electrochemical performance, Electrochem. Energy Rev. 6 (1) (2023) 18, http://dx.doi.org/10.1007/s41918-022-00157-3.

[14] L. Johnson, C. Li, Z. Liu, Y. Chen, S.A. Freunberger, P.C. Ashok, B.B. Praveen, K. Dholakia, J.M. Tarascon, P.G. Bruce, The role of LiO₂ solubility in O₂ reduction in aprotic solvents and its consequences for Li–O₂ batteries, Nat. Chem. 6 (12) (2014) 1091–1099, http://dx.doi.org/10.1038/NCHEM.2101.

[15] M. Park, H. Sun, H. Lee, J. Lee, J. Cho, Lithium–air batteries: Survey on the current status and perspectives towards automotive applications from a battery industry standpoint, Adv. Energy Mater. 2 (7) (2012) 780–800, http://dx.doi.org/10.1002/aenm.201200020.

[16] N. Feng, P. He, H. Zhou, Critical challenges in rechargeable aprotic Li–O₂ batteries, Adv. Energy Mater. 6 (9) (2016) 1502303, http://dx.doi.org/10.1002/aenm.201502303.

[17] Z. Lyu, Y. Zhou, W. Dai, X. Cui, M. Lai, L. Wang, F. Huo, W. Huang, Z. Hu, W. Chen, Recent advances in understanding of the mechanism and control of Li₂O₂ formation in aprotic Li–O₂ batteries, Chem. Soc. Rev. 46 (19) (2017) 6046–6072, http://dx.doi.org/10.1039/c7cs00255f.

[18] E.J. Askins, M.R. Zoric, M. Li, R. Amine, K. Amine, L.A. Curtiss, K.D. Glusac, Triarylmethyl cation redox mediators enhance Li–O₂ battery discharge capacities, Nature Chem. 15 (9) (2023) 1247–1254, http://dx.doi.org/10.1038/s41557-023-01268-0.

[19] J.B. Park, S.H. Lee, H.G. Jung, D. Aurbach, Y.K. Sun, Redox mediators for Li–O₂ batteries: status and perspectives, Adv. Mater. 30 (1) (2018) 1704162, http://dx.doi.org/10.1002/adfm.201808303.

[20] M. Balaish, J.W. Jung, I.D. Kim, Y. Ein Eli, A critical review on functionalization of air-cathodes for nonaqueous Li–O₂ batteries, Adv. Funct. Mater. 30 (18) (2020) 1808303, http://dx.doi.org/10.1002/adfm.201808303.

[21] A. Kushima, T. Koido, Y. Fujiwara, N. Kuriyama, N. Kusumi, J. Li, Charging/discharging nanomorphology asymmetry and rate-dependent capacity degradation in Li–oxygen battery, Nano Lett. 15 (12) (2015) 8260–8265, http://dx.doi.org/10.1021/acs.nanolett.5b03812.

[22] S. Lau, L.A. Archer, Nucleation and growth of lithium peroxide in the Li–O₂ battery, Nano Lett. 15 (9) (2015) 5995–6002, http://dx.doi.org/10.1021/acs.nanolett.5b02149.

[23] M. Kim, E. Yoo, W.-S. Ahn, S.E. Shim, Controlling porosity of porous carbon cathode for lithium oxygen batteries: Influence of micro and meso porosity, J. Power Sources 389 (2018) 20–27, http://dx.doi.org/10.1016/j.jpowsour.2018.03.080.

[24] A. Dutta, R.A. Wong, W. Park, K. Yamanaka, T. Ohta, Y. Jung, H.R. Byon, Nanostructuring one-dimensional and amorphous lithium peroxide for high round-trip efficiency in lithium–oxygen batteries, Nature Commun. 9 (1) (2018) 680, http://dx.doi.org/10.1038/s41467-017-02727-2.

[25] A. Dutta, K. Ito, Y. Kubo, Establishing the criteria and strategies to achieve high power during discharge of a Li–air battery, J. Mater. Chem. A 7 (40) (2019) 23199–23207, http://dx.doi.org/10.1021/acsaem.9b02237.

[26] B. Liu, W. Xu, J. Zheng, P. Yan, E.D. Walter, N. Isern, M.E. Bowden, M.H. Engelhard, S.T. Kim, J. Read, et al., Temperature dependence of the oxygen reduction mechanism in nonaqueous Li–O₂ batteries, ACS Energy Lett. 2 (11) (2017) 2525–2530, http://dx.doi.org/10.1021/acsenergylett.7b00845.

[27] X. Gao, Y. Chen, L. Johnson, P.G. Bruce, Promoting solution phase discharge in Li–O₂ batteries containing weakly solvating electrolyte solutions, Nat. Mater. 15 (8) (2016) 882–888, http://dx.doi.org/10.1002/adfm.201808303.

[28] X. Gao, Y. Chen, L.R. Johnson, Z.P. Jovanov, P.G. Bruce, A rechargeable lithium–oxygen battery with dual mediators stabilizing the carbon cathode, Nat. Energy 2 (9) (2017) 1–7, http://dx.doi.org/10.1038/nenergy.2017.118.

[29] M. Asadi, B. Sayahpour, P. Abbasi, A.T. Ngo, K. Karis, J.R. Jokisaari, C. Liu, B. Narayanan, M. Gerard, P. Yasaei, et al., A lithium–oxygen battery with a long cycle life in an air-like atmosphere, Nature 555 (7697) (2018) 502–506, http://dx.doi.org/10.1038/nature25984.

[30] K. Chen, G. Huang, J.-L. Ma, J. Wang, D.-Y. Yang, X.-Y. Yang, Y. Yu, X.-B. Zhang, The stabilization effect of CO₂ in lithium–oxygen/CO₂ batteries, Angew. Chem. Int. Ed. 59 (38) (2020) 16661–16667, http://dx.doi.org/10.1002/ange.202006303.

[31] P. Tan, W. Kong, Z. Shao, M. Liu, M. Ni, Advances in modeling and simulation of Li–air batteries, Prog. Energy Combust. Sci. 62 (2017) 155–189, http://dx.doi.org/10.1016/j.pecs.2017.06.001.

[32] C.Y. Jung, T.S. Zhao, L. An, Modeling of lithium–oxygen batteries with the discharge product treated as a discontinuous deposit layer, J. Power Sources 273 (2015) 440–447, http://dx.doi.org/10.1016/j.jpowsour.2014.09.103.

[33] J. Liu, S.K. Rahimian, C.W. Monroe, Capacity-limiting mechanisms in Li/O₂ batteries, Phys. Chem. Chem. Phys. 18 (33) (2016) 22840–22851, http://dx.doi.org/10.1039/c6cp04055a.

[34] C. Gaya, Y. Yin, A. Torayev, Y. Mammeri, A.A. Franco, Investigation of bi-porous electrodes for lithium oxygen batteries, Electrochim. Acta 279 (2018) 118–127, http://dx.doi.org/10.1016/j.electacta.2018.05.056.

[35] K. Jiang, X. Liu, G. Lou, Z. Wen, L. Liu, Parameter sensitivity analysis and cathode structure optimization of a non-aqueous Li–O₂ battery model, J. Power Sources 451 (2020) 227821, http://dx.doi.org/10.1016/j.jpowsour.2020.227821.

[36] A.V. Sergeev, A.V. Chertovich, D.M. Itkis, E.A. Goodilin, A.R. Khokhlov, Effects of cathode and electrolyte properties on lithium–air battery performance: Computational study, J. Power Sources 279 (2015) 707–712, http://dx.doi.org/10.1016/j.jpowsour.2015.01.024.

[37] F. Wang, X. Li, X. Hao, J. Tan, A modeling study of discharging Li–O₂ batteries with various electrolyte concentrations, J. Electrochem. Energy Convers. Storage 18 (1) (2021) 011009, http://dx.doi.org/10.1115/1.4046931.

[38] T. Zhang, M. Yu, J. Li, Q. Li, X. Zhang, H. Sun, Effect of porosity gradient on mass transfer and discharge of hybrid electrolyte lithium–air batteries, J. Energy Storage 46 (2022) 103808, http://dx.doi.org/10.1016/j.est.2021.103808.

[39] G. Gwak, H. Ju, Three-dimensional transient modeling of a non-aqueous electrolyte lithium–air battery, Electrochim. Acta 201 (2016) 395–409, http://dx.doi.org/10.1016/j.electacta.2016.03.040.

[40] Y. Gao, W. Zhou, Z. Wen, R. Dou, X. Liu, Meso-scale simulation of Li–O₂ battery discharge process by an improved lattice Boltzmann method, Electrochim. Acta 442 (2023) 141880, http://dx.doi.org/10.1016/j.electacta.2023.141880.

[41] Y.-X. Yu, Effect of defects and solvents on silicene cathode of nonaqueous lithium–oxygen batteries: a theoretical investigation, J. Phys. Chem. C 123 (1) (2019) 205–213, http://dx.doi.org/10.1021/acs.jpcc.8b10367.

[42] J.-H. Li, Y.-X. Yu, Enhanced catalytic performance of pillared δ-MnO₂ with enlarged layer spaces for lithium–and sodium–oxygen batteries: a theoretical investigation, Nanoscale 13 (48) (2021) 20637–20648, http://dx.doi.org/10.1039/d1nr07407e.

[43] J.-H. Li, J. Wu, Y.-X. Yu, Theoretical exploration of single-layer Tl₂O as a catalyst in lithium–oxygen battery cathodes, J. Phys. Chem. C 124 (17) (2020) 9089–9098, http://dx.doi.org/10.1021/acs.jpcc.9b09665.

[44] Q. Li, K.H. Luo, Q.J. Kang, Y.L. He, Q. Chen, Q. Liu, Lattice Boltzmann methods for multiphase flow and phase-change heat transfer, Prog. Energy Combust. Sci. 52 (2016) 62–105, http://dx.doi.org/10.1016/j.pecs.2015.10.001.

[45] T. Lei, K.H. Luo, Lattice Boltzmann simulation of multicomponent porous media flows with chemical reaction, Front. Phys. 9 (2021) 715791, http://dx.doi.org/10.3389/fphy.2021.715791.

[46] L. Chen, R. Zhang, Q. Kang, W.Q. Tao, Pore-scale study of pore-ionomer interfacial reactive transport processes in proton exchange membrane fuel cell catalyst layer, Chem. Eng. J. 391 (2020) 123590, http://dx.doi.org/10.1016/j.cej.2019.123590.

[47] D. Zhang, A. Forner-Cuenca, O.O. Taiwo, V. Yufit, F.R. Brushett, N.P. Brandon, S. Gu, Q. Cai, Understanding the role of the porous electrode microstructure in redox flow battery performance using an experimentally validated 3D pore-scale lattice Boltzmann model, J. Power Sources 447 (2020) 227249, http://dx.doi.org/10.1016/j.jpowsour.2019.227249.

[48] S. Wan, X. Liang, H. Jiang, J. Sun, N. Djilali, T. Zhao, A coupled machine learning and genetic algorithm approach to the design of porous electrodes for redox flow batteries, Appl. Energy 298 (2021) 117177, http://dx.doi.org/10.1016/j.apenergy.2021.117177.

[49] T. Lai, Z. Qu, Pore-scale parametric sensitivity analysis of liquid water transport in the gas diffusion layer of polymer electrolyte membrane fuel cell, Appl. Therm. Eng. 229 (2023) 120616, http://dx.doi.org/10.1016/j.applthermaleng.2023.120616.

[50] S. Park, M.-H. Kim, S. Um, Phase separation modeling of water transport in polymer electrolyte membrane fuel cells using the Multiple-Relaxation-Time lattice Boltzmann method, Chem. Eng. J. 495 (2024) 153629, http://dx.doi.org/10.1016/j.cej.2024.153629.

[51] W.Z. Fang, R. Qiao, Q. Kang, W.Q. Tao, Pore-scale simulation of reactive transport processes in lithium–oxygen batteries, Int. Commun. Heat Mass Transfer 129 (2021) 105740, http://dx.doi.org/10.1016/j.icheatmasstransfer.2021.105740.

[52] J. Yang, T. Lei, G. Wang, Q. Xu, J. Chen, K.H. Luo, Lattice Boltzmann modelling of salt precipitation during brine evaporation, Adv. Water Resour. 180 (2023) 104542, http://dx.doi.org/10.1016/j.advwatres.2023.104542.

[53] C.P. Andersen, H. Hu, G. Qiu, V. Kalra, Y. Sun, Pore-scale transport resolved model incorporating cathode microstructure and peroxide growth in lithium–air batteries, J. Electrochem. Soc. 162 (7) (2015) A1135, http://dx.doi.org/10.1149/2.0051507jes.

[54] T. Lei, K.H. Luo, F.E. Hernández Pérez, G. Wang, Z. Wang, J. Restrepo Cano, H.G. Im, Study of CO_2 desublimation during cryogenic carbon capture using the lattice Boltzmann method, J. Fluid Mech. 964 (2023) A1, http://dx.doi.org/10.1017/jfm.2023.227.

[55] Q.J. Kang, L. Chen, A.J. Valocchi, H.S. Viswanathan, Pore-scale study of dissolution-induced changes in permeability and porosity of porous media, J. Hydrol. 517 (2014) 1049–1055, http://dx.doi.org/10.1016/j.jhydrol.2014.06.045.

[56] T. Lei, Z. Wang, K.H. Luo, Study of pore-scale coke combustion in porous media using lattice Boltzmann method, Combust. Flame 225 (2021) 104–119, http://dx.doi.org/10.1016/j.combustflame.2020.10.036.

[57] T. Lei, K.H. Luo, Pore-scale study of dissolution-driven density instability with reaction $A + B \rightarrow C$ in porous media, Phys. Rev. Fluids 4 (6) (2019) 063907, http://dx.doi.org/10.1103/PhysRevFluids.4.063907.

[58] Z.L. Guo, C. Shu, Lattice Boltzmann Method and Its Applications in Engineering, World Scientific Publisher, Singapore, Singapore, 2013, pp. 25–28,76–78,329–338.

[59] Y.C. Lu, D.G. Kwabi, K.P. Yao, J.R. Harding, J. Zhou, L. Zuin, Y. Shao Horn, The discharge rate capability of rechargeable $Li–O_2$ batteries, Energy Environ. Sci. 4 (8) (2011) 2999–3007, http://dx.doi.org/10.1039/C1EE01500A.

[60] W.H. Ryu, F.S. Gittleson, J. Li, X. Tong, A.D. Taylor, A new design strategy for observing lithium oxide growth-evolution interactions using geometric catalyst positioning, Nano Lett. 16 (8) (2016) 4799–4806, http://dx.doi.org/10.1021/acs.nanolett.6b00856.

[61] J. Read, Characterization of the lithium/oxygen organic electrolyte battery, J. Electrochem. Soc. 149 (9) (2002) A1190, http://dx.doi.org/10.1149/1.1498256.

[62] C.X. Pan, L.S. Luo, C.T. Miller, An evaluation of lattice Boltzmann schemes for porous medium flow simulation, Comput. & Fluids 35 (8–9) (2006) 898–909, http://dx.doi.org/10.1016/j.compfluid.2005.03.008.

[63] Q.J. Kang, P.C. Lichtner, D.X. Zhang, Lattice Boltzmann pore-scale model for multicomponent reactive transport in porous media, J. Geophys. Res.: Solid Earth 111 (B5) (2006) B05203, http://dx.doi.org/10.1029/2005JB003951.